

A Space-based Decametric Wavelength Radio Telescope Concept

K. Belov¹, A. Branch¹, S. Broschart¹, J. Castillo-Rogez¹, S. Chien¹, L. Clare¹, R. Dengler¹,
J. Gao¹, D. Garza¹, A. Hegedus^{1,2}, S. Hernandez¹, S. Herzig¹, T. Imken¹, H. Kim¹,
S. Mandutianu¹, A. Romero-Wolf¹, S. Schaffer¹, M. Troesch¹, E.J. Wyatt¹, J. Lazio¹

¹*Jet Propulsion Laboratory, California Institute of Technology, Pasadena, CA 91109, USA*

²*Climate and Space Sciences and Engineering Department,
University of Michigan, Ann Arbor, MI 48109-2143, USA*

(Dated: August 21, 2021)

This paper reports a design study for a space-based decametric wavelength telescope. While not a new concept, this design study focused on many of the operational aspects that would be required for an actual mission. This design optimized the number of spacecraft to insure good visibility of approx. 80% of the radio galaxies— the primary science target for the mission. A 5,000 km lunar orbit was selected to guarantee minimal gravitational perturbations from Earth and lower radio interference. Optimal schemes for data downlink, spacecraft ranging, and power consumption were identified. An optimal mission duration of 1 year was chosen based on science goals, payload complexity, and other factors. Finally, preliminary simulations showing image reconstruction were conducted to confirm viability of the mission. This work is intended to show the viability and science benefits of conducting multi-spacecraft networked radio astronomy missions in the next few years.

I. INTRODUCTION

The discovery by K. Jansky of celestial radio emission occurred at a radio frequency of 20.5 MHz [1], and discoveries at low radio frequencies ($\nu \lesssim 100$ MHz) have helped form much of the basis for modern astronomy. Low radio frequency observations have also pioneered key technical improvements, most notably the development of aperture synthesis interferometry [2–7]. Subsequent to these early discoveries, a number of large, low radio frequency telescopes were constructed, and the field has undergone something of a recent renaissance with several telescopes being either constructed or upgraded.

A fundamental limitation to ground-based radio astronomy is the Earth’s ionosphere. Radio waves propagating through the ionosphere exhibit measurable phase changes at frequencies even well above 1 GHz, and, at frequencies below about 100 MHz, there is increasing absorption. The frequency at which the ionosphere becomes opaque varies both with location (due to the structure of the Earth’s magnetic field) and time (e.g., diurnal effects, solar cycle), but the cutoff frequency is generally taken to be about 10 MHz. While there have been impressive efforts to make ground-based measurements at lower frequencies [e.g., 8–11], the detrimental effects of the ionosphere also are reflected in the fact that the International Telecommunications Union provides no recommendations for radio astronomical observations below 13.6 MHz [12].

At lower frequencies, space-based observations are required, and radio receivers are a common instrument on both planetary and heliospheric spacecraft [e.g., 13–16]. There have also been two missions dedicated to radio astronomical observations of objects beyond the solar system. The first Radio Astronomy Explorer (RAE-1) was in an Earth orbit and made the first measurements of the Galaxy’s spectrum between 0.4 and 6.5 MHz [17] while the second Radio Astronomy Explorer (RAE-2) was in a lunar orbit and observed between 25 kHz and 13 MHz [18].

On the ground, there have been numerous large interferometric arrays, designed to provide higher sensitivity and imaging performance than can be realized with a single antenna, including the Giant Metrewave Radio Telescope [19, 20], the 74 MHz Very Large Array [21], the Ukrainian T-shaped Radio Telescope [UTR-2, 22], Low Frequency Array [23], the Long Wavelength Array [24, 25], and the Murchison Widefield Array [26]. There have been initial descriptions and proposals of concepts for space-based radio astronomical arrays [e.g., 27–31], notably including the Astronomical Low Frequency Array (ALFA) mission concept [32], “cubesat”-based arrays [33], OLFAR [34], DSL [35] and NOIRE [36]. Proofs of concept of a space-based radio interferometric array have been conducted by observing the Earth’s auroral kilometric radiation with a single-element interferometer consisting of the ISEE-1 and ISEE-2 spacecraft [37] and a time-difference-of-arrival (TDOA) analysis with the Cluster spacecraft [38].

Recent standardization of small (“cubesat”) spacecraft components may now make a space-based radio interferometric array feasible. Further, the instrumentation required for detecting radio frequencies below 15 MHz is relatively simple and amenable to a small spacecraft. However, a recognized challenge for implementing a “constellation” of small spacecraft, such as would be required for a space-based array, is the telecommunications either between spacecraft or from the spacecraft to the Earth. This paper reports on a concept study designed to explore and develop solutions for implementing a space-based array (Figure 1), with a primary focus is on the telecommunications (“telecomm”) and

operations. In §II, we summarize a motivating science case for a space-based array and the resulting requirements; in §IV, we summarize strawman spacecraft designs; in §III, we present the mission design; in §V, we comment briefly on aspects related to using the transmitted data to form the desired radio astronomical images; and, in §VI, we present our conclusions. Appendix A presents a more detailed description of the radio receiving system for the science data collection. For consistency with the concept described in [39], we retain its name of RELIC.

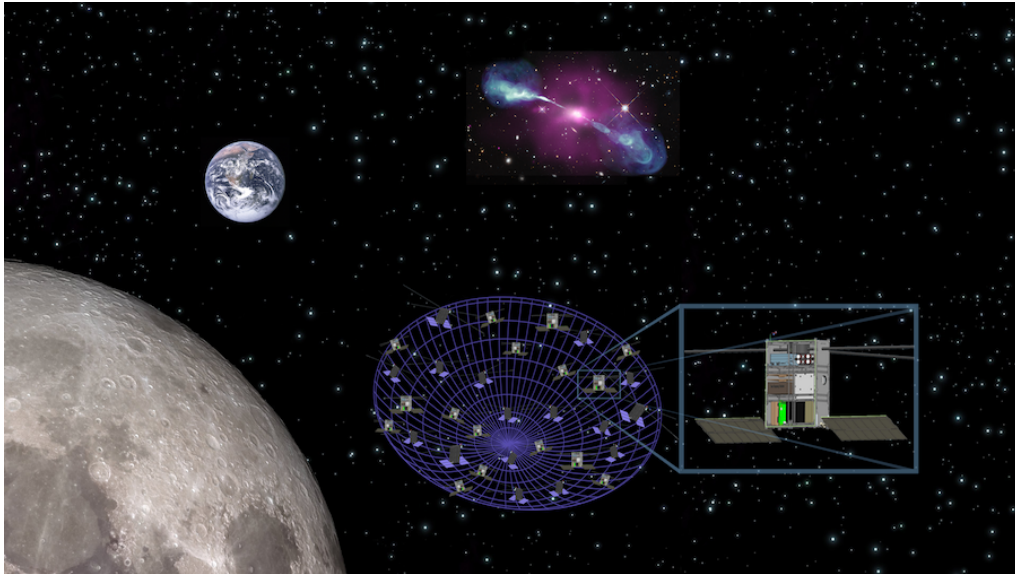


FIG. 1: Artist's impression of the RELIC constellation. For clarity, the mothership is not pictured.

II. SCIENCE DEFINITION AND MISSION DESIGN REQUIREMENTS

The potential science cases for a space-based array have been well described in previous discussions of such a concept [e.g., 27, 28, 31–35, 40, 41].

The science cases cover a large range of topics including radio emission from energetic particles in the inner heliosphere, magnetospheric emissions from solar system planets with planetary-scale magnetic fields, and, potentially in the future, studying magnetospheric emissions from extrasolar planets. While we considered the above mentioned cases, we choose to focus on a specific science case, namely the imaging of radio galaxies. This choice is motivated in part by the identification of this science case as one that forms a key part of a multi-wavelength study of physical processes in active galaxies [39] and in part because this science case produces requirements that are more broadly applicable to a number of other science cases.

In brief, the combination of synchrotron and inverse Compton emission, the former measured at radio wavelengths and the latter measured at X-ray wavelengths, provide information on the plasma and magnetic field properties in regions where particles are being accelerated or as they stream away from those regions. Ground-based measurements can be used to measure a portion of the synchrotron spectrum [e.g., 42, 43], but access to the radio spectrum at 10 MHz or lower would reduce uncertainties substantially by limiting the extent to which the electron energy distribution has to be extrapolated in energy. In order to have some overlap with ground-based observations, we specify a frequency range below 30 MHz.

In order to set high-level science requirements for the RELIC concept, we selected the nearest 85 double radio sources associated with a galactic nuclei (DRAGNs) from the 3CR sample [44]. Figures 2 and 3 summarize the range of angular scales observed in DRAGNs, with the mean size being approximately $100''$ and 80% of the sources being in the range $10''$ to $500''$. In addition to the intrinsic sizes of DRAGNs, at the frequencies of interest, significant angular broadening due to density fluctuations in the interstellar medium occurs [48]. This propagation effect limits to approximately $10''$ the finest angular resolution that is required.

Figure 4 shows the distribution of flux densities at 10 MHz for our sample. In order to estimate these flux densities, we scaled the measured flux densities from their measured values at 178 MHz assuming a spectrum of $S \propto \nu^\alpha$, with $\alpha = -0.7$. This scaling assumes that there is no free-free absorption due to a foreground thermal population of electrons. Some surveys show significant variations of the scaling for different sources [49]. There is some evidence of

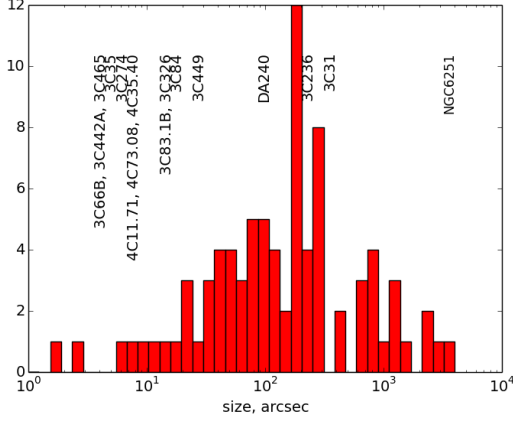


FIG. 2: DRAGN size distribution from the 3CR [44].

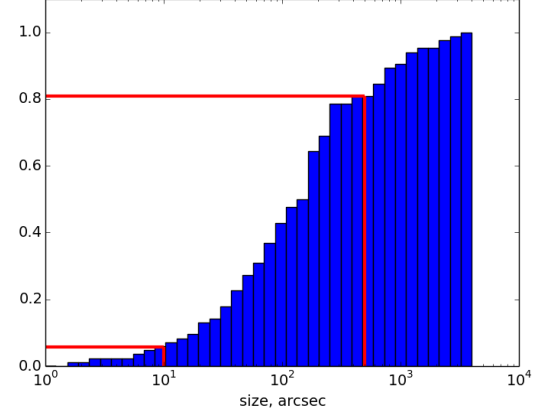


FIG. 3: Cumulative distribution of DRAGN angular sizes. The red lines demarcate the range encompassing approximately 80% of the sources.

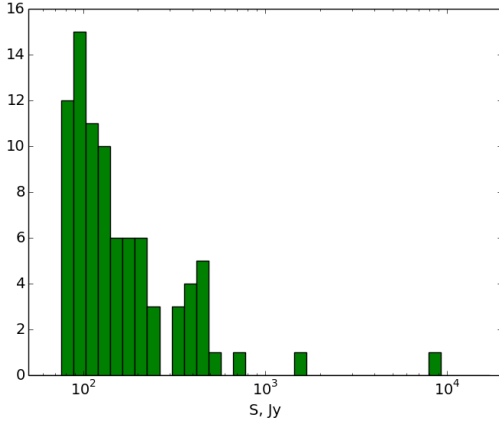


FIG. 4: Flux densities of our double radio sources associated with a galactic nuclei (DRAGNs) sample, as selected from the 3CR survey and scaled to 10 MHz. The truncation at low flux densities represents the completeness limit of the parent catalog from which our sample is drawn.

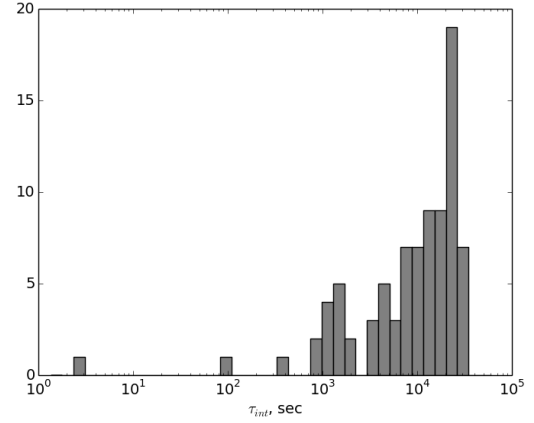


FIG. 5: DRAGN integration time at 10 MHz. The calculation is based on the flux densities shown in Figure 4

the Cygnus A hotspot spectrum turn over at lower frequencies [45], but generally, the radio emission of interest from these DRAGNs is from well outside the main stellar disk of the host galaxy and they are at high Galactic latitudes, meaning that this assumption should be valid for the vast majority, if not all, of our sample.

Table I summarizes these science requirements for the RELIC mission concept.

Table II summarizes the high-level mission requirements that are derived from the science requirements (Table I).

A fundamental telescope architecture question is whether it should be monolithic (i.e., completely filled aperture) or segmented; we consider an interferometer to be an extreme example of a segmented telescope. Simple optics considerations show that, in order to obtain the required angular resolution at the relevant frequencies, an effective aperture exceeding 100 km in diameter is required. Consequently, we henceforth adopt an interferometric design for the telescope.

The maximum angular resolution of the array is limited to $\sim 10''$ by the interstellar broadening [48]. At 10 MHz this corresponds to 620 km longest projected baseline, which already presents significant communication challenges, limiting the available data bandwidth. The dilution of the angular resolution can also be due to uncertainty in the asset location positing and due to the clock drift, which imposes corresponding hardware requirements. In order to provide the best source visibility, the minimum spacecraft (S/C) separation should be less than 12 km, as the largest radio galaxies are about $30'$ in size. The baseline mission architecture is one *mothership* with 32 *daughterships*

TABLE I: Science Driven Requirements

Requirement	Science	Implied Mission Requirements
Angular resolution	$10''^a$	620 km max S/C separation
Largest angular scale	$30'^b$	12 km min S/C separation Non-repeating baselines 32 S/C minimum
Frequency bandwidth	0.1-10 MHz + 30 MHz Best science < 10 MHz Overlap with ground: 30 MHz	Data rate
Image S/N ratio	10	Min source obs. time 3 hours

^aLimited by interstellar broadening^bAngular size of a large radio galaxy

TABLE II: Requirements driven by mission design considerations.

Parameter	Value	Rationale
Frequency resolution	16 kHz	See sec. III E 2
Spectral windows	> 64	See sec. III E 3
Dynamic range	10^3 – 10^4	S/N ratio, see table I and sec. III E 1
Polarizations	2	See below in this section
Sessions per source	1–3 hour ^a	Can be split into mult. sessions

^aOr multiple sessions totaling ~ 3 hours

delivered to the initial orbits by a single launch vehicle. Given a target flux density, a target S/N ratio, and a notional integration time, see Figures 4 and 5, an array composed of 32 dual-polarization antennas is sufficient to detect a typical source.

Each S/C should carry a dual-polarization dipole, i.e., be capable of receiving both polarization, in order to provide an additional $\sqrt{2}$ improvement in signal-to-noise ratio and to provide redundancy for each S/C. In addition, signal polarization is a powerful means of rejecting terrestrial interference. Not considered in this trade study was a cost-benefit analysis of each S/C carrying a so-called tripole system in order to capture the full three-dimensional information about the electric field [e.g., 46], but one immediately obvious cost of carrying a tripole antenna system on each S/C would be an increased data rate requirement. One design solution for a tripole antenna is described in details in [47]

Finally, the mission should allow for the S/C pointing to keep the sources in the FOV during a session long enough to establish an interferometric image. The orbits are discussed in details in the section III B below. The ability to sample signal up to 30 MHz is desirable to overlap with the ground observations. This requirement dictates the sampling rate of 60 MHz and a broadband antenna, the exact design of which will be chosen later. Anticipating future results as discussed below, we consider the observation bandwidth to be 16 kHz. Each daughtership performs very limited data processing, downlinking the data to the mothership for further processing and further downlinking to the ground. This architecture is a compromise between the limited bandwidth for the data transfer to the mothership, limited power available to the daughtership and limited or non-existent daughtership to daughtership intercom.

III. MISSION ARCHITECTURE

A. Design Optimization Using Operations Analysis

One of the challenges in space mission design is correctly accounting for a large number of design dimensions that may interact in subtle and hard to predict ways. We address this difficulty by adopting an operations-based approach to evaluating mission designs. We in effect partially simulate the missions, applying any and all operations constraints we can to derive results as realistic as possible. We characterize the science measurements possible and use these as a proxy for mission return. By performing these simulations and calculations, we aim to estimate mission return and therefore enable devoting resources to the most promising early mission designs.

In this section we discuss our implementation and results, focusing on a data throughput analysis to estimate mission lifetime to fulfill its main scientific goals.

1. Data Throughput Analysis Using Operations Planning

The data throughput analysis is performed using the ASPEN/CASPER planning system [50, 51]. ASPEN is a timeline-based scheduling framework that allows for operations, S/C, science, and other constraints to be incorporated in an automated scheduling environment. The automatic scheduling algorithms generate a proposed mission operations schedule following a set of constraints. The generated mission plans may then be evaluated for various metrics such as science data utility and remaining resource margins.

The planner leverages a common core of action/state models. The actions available in the common model span the entire constellation: some are executed only on individual daughterships, some only on the mothership, and others require joint simultaneous action by multiple spacecraft. The modeled actions include repointing the daughterships, science data acquisition, crosslinking data from a daughtership to the mothership, downlinking data from the mothership to Earth, downlinking data directly from a daughtership to Earth, and placeholders for intermittently required engineering activities. These actions make use of various modeled states and resources including the visibility of each science target, the interferometric baseline utility of each observation window, the number of receivers on the mothership, the visibility of Deep Space Network ground stations, the bandwidth of each communication link, power generation rate, and remaining battery reserves.

The CASPER automated operations planning system then uses the combined core model and design constraints to generate a proposed operations plan. CASPER starts from an empty mission plan and iteratively optimizes it by adding or removing actions to improve a declared utility function. The utility function is directly related to the calculated science utility of the data received at Earth, and strongly inversely related to any mission constraint violations. This approach guides the planner to add observation, crosslink, and downlink activities while respecting the design limits on view periods, storage space, bandwidth, power, and other similar constraints. The calculated utility of the science data is related to the total observation integration time and how well the selected interferometry baselines cover the space of distances and angles needed to characterize the structure of each radio astronomy target. The final output operations schedule from the planner includes concrete timed actions for each of the constellation craft to execute.

Critical to all of this operations planning is the geometric aspect of the problem. For all of these geometric analyses, we use the SPICE package [52]. These analyses include daughtership position and science target position for array analysis, daughtership and mothership position for crosslink calculations, and mothership and ground station position and downlink calculation.

The operations schedule can then be evaluated versus specified metrics. Primary metrics are the uv-plane coverage, integration time, and target coverage. Additional metrics such as excess unused capacity on some resources (e.g., unused power or bandwidth) are also reported to help inform which parts of a design may be over-engineered and which are the bottlenecks during actual operations. For the data throughput analysis, the duration of crosslink, downlink, and observation activities are of interest.

Figure 6 shows the amount of time that would be required for science data acquisition, crosslink from daughtership to mothership, and downlink from mothership to Earth, all determined using the approach described above. It is clear that crosslinking would be the most costly action in terms of mission duration, requiring roughly 10 mission days per observation day. The crosslink time also would increase significantly with the separation of the daughterships, while the observation time and the downlink time would remain constant. As the daughterships move further away from the mothership, assumed to be at the center of the array, the available bandwidth for crosslinking decreases. One technique to offset the decrease is mentioned below.

B. Orbit Selection and Modeling

The baseline orbit design is a mothership orbiting in a circular orbit with an altitude of 5000 km above the Moon and 32 daughterships orbiting around the mothership in a cluster. The number of daughterships was chosen to serve as a “baseline” to obtain an adequate uv-plane coverage from a preliminary analysis with several major assumptions made about the hardware. Once the hardware design is finalized during the mission proposal study, a more accurate modeling will be possible. The mothership orbit was chosen for science purposes to be far enough from the Earth to avoid interference, as well as minimize gravitational perturbations from Earth. Figure 7 shows a dynamic spectrum from the Wind/WAVES instrument, when the Wind spacecraft was approximately at one lunar distance on April 2, 1999. While there is some ionospheric breakout, below 5 MHz, there is essentially no terrestrial RFI. Even above 5 MHz, there are still relatively clean bands at least up to 10 MHz.

Due to perturbations from Earth and Sun, the chosen orbits vary in inclination over the course of time, from -30 deg. To +30 approximately. Although not required by the mission, the brief periods of RFI shielding from Earth are an added benefit. The maximum allowed baseline between any two daughterships for science is approximately

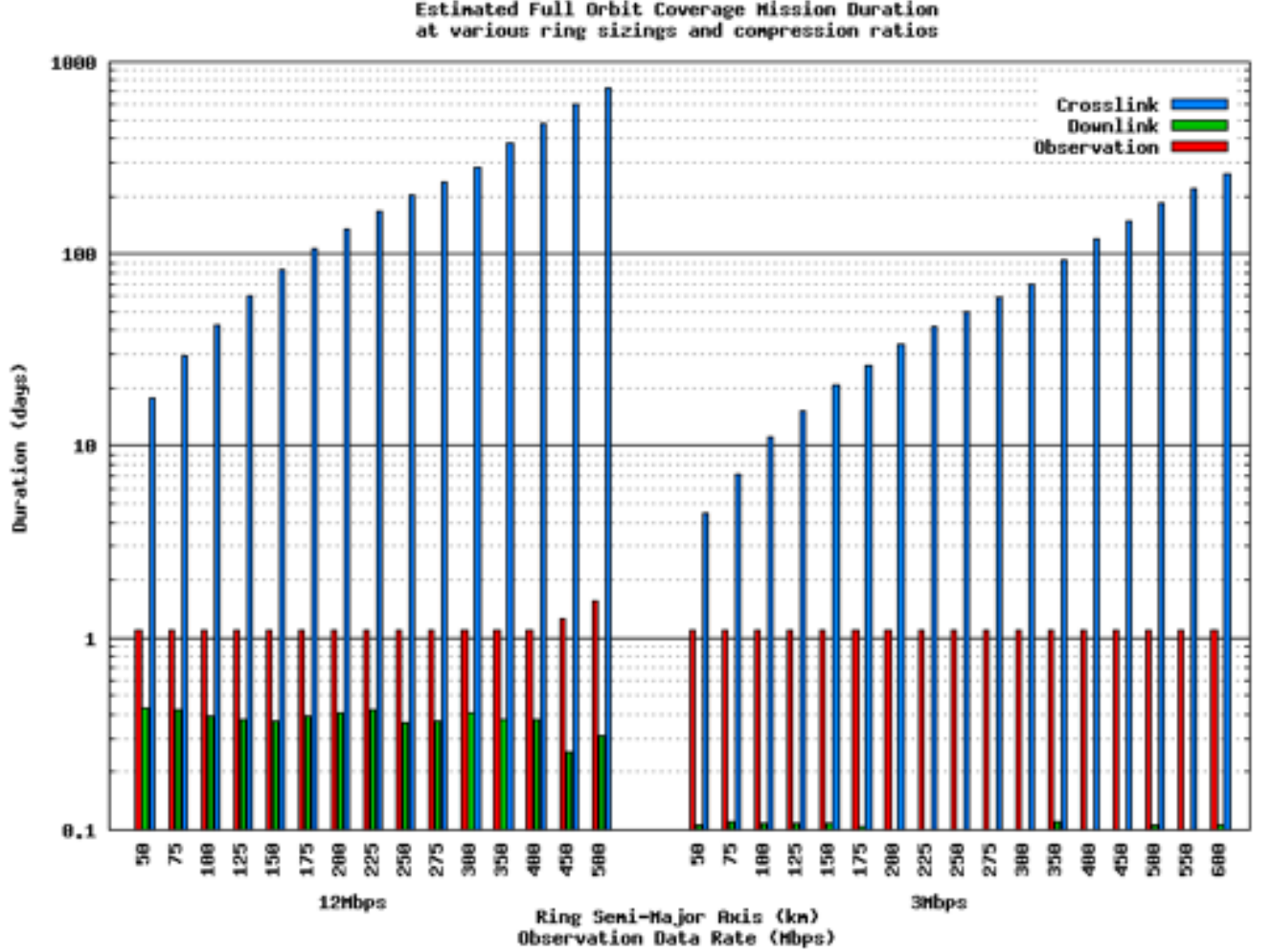


FIG. 6: Intervals for relevant activities per day of observation as a function of crosslink data rate and maximum separation between daughterships, with the different color bars indicating the different activities—crosslink (blue), downlink (green), and observation (red).

600 km; therefore, the entire cluster needs to remain relatively close (Figure 8a). For this reason, the orbits of all the daughterships are designed to have the same period (≈ 8.8 hr), with slightly varying eccentricity and inclination. In a relative, rotating frame fixed at the mothership, the equal period orbits are accomplished by 2×1 ellipses of varying sizes and centers, mimicking a “gear-like” movement, which allows for optimum uv-plane coverage (Figure 8b). We henceforth term these ellipses on which the daughterships would be orbiting as “rings.”

As the orbital period is constant, after one full revolution around the Moon, the daughterships all would return to the initial relative configuration, i.e., same location in Figure 8b. Most of the science and data downlink could be accomplished within a few orbits around the Moon for a specific configuration. Because the structure of the target radio galaxies is not expected to change significantly on the time scale for this mission, it is possible to improve the aperture plane coverage by reconfiguring each ring to change its size. This technique is conceptually similar to the practice used in early efforts to reconstruct the brightness distribution of radio galaxies [53–55] and continues to be used to date, e.g., combining data from multiple configurations of the Very Large Array. The main constraint is to maintain the same orbit period for all daughterships, which can be accomplished only via a maneuver perpendicular to the velocity direction. For each ring, the maneuver for reconfiguration would happen at the same location in the relative orbit, ensuring that all daughterships reconfigure to the same ring. It takes about one orbit revolution to reconfigure all daughterships on one ring. Reconfiguration should happen sequentially from largest to smallest ring in order to minimize the risk of collisions. The daughterships could reconfigure as many times as needed, within a given ΔV budget.

The final design chosen is four rings, with 8 daughterships in each ring. Each daughtership would deploy from the

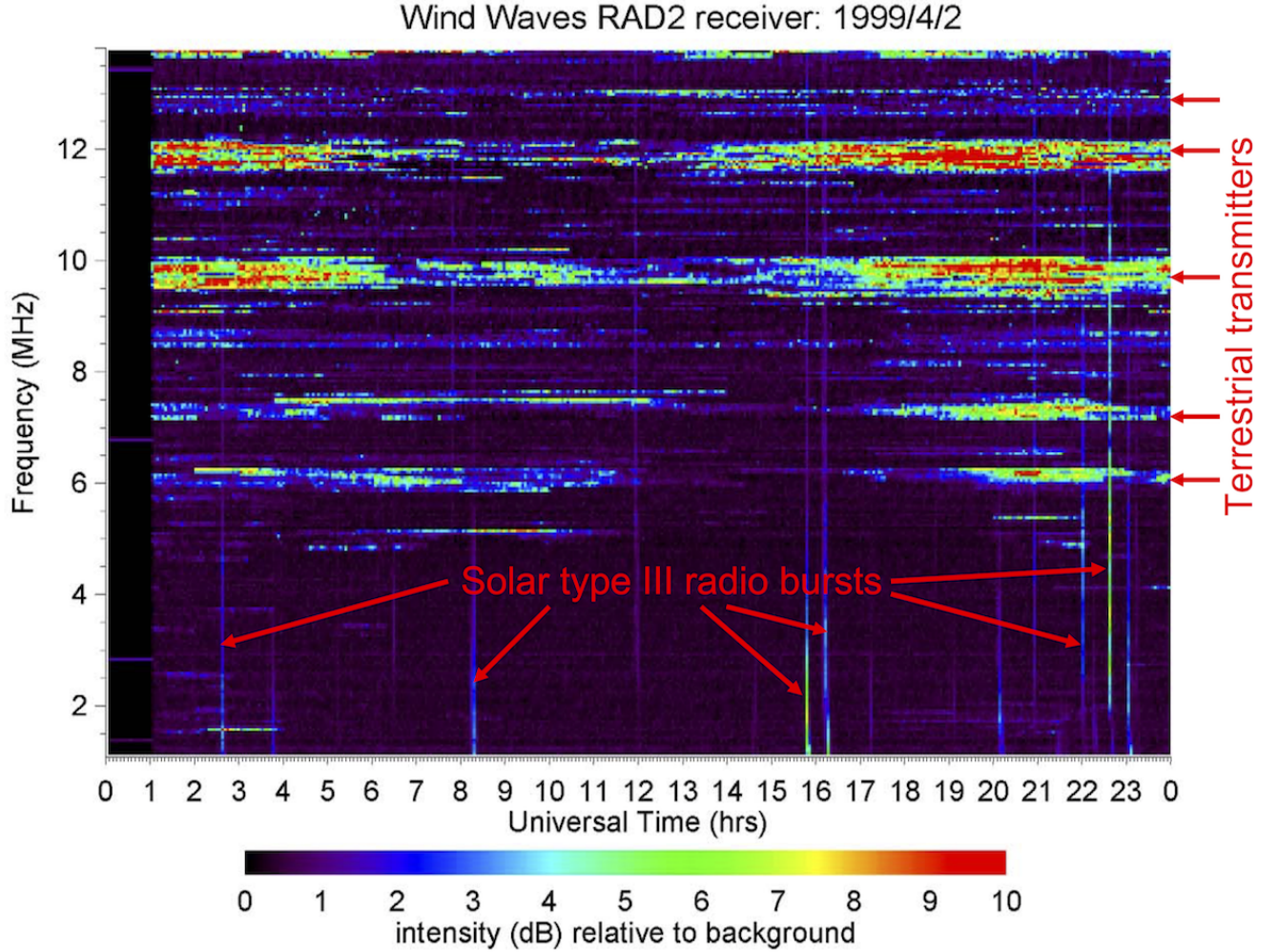


FIG. 7: Dynamic spectrum from the Wind/WAVES instrument, when the Wind spacecraft was approximately at one lunar distance on April 2, 1999. NASA/GSFC, R. MacDowall..

mothership sequentially to its initial configuration (Figure 9[a]; Table III). The mothership is at the center of the formation. The initial configuration of the rings has been designed to cost 20 m s^{-1} for each daughtership. After all the science data has been gathered and downlinked to Earth within a specific configuration, the daughterships would reconfigure, applying 1 m s^{-1} perpendicular to their velocity, which allows for 5 km increase in ring size.

Such a ring reconfiguration could be obtained if each daughtership carries a 1 N thruster capable of generating a specific impulse of at least $I_s = 200 \text{ s}$ (§IV). A total of 20 reconfigurations (equivalent to 20 m s^{-1} of propellant) could be applied, ending in the final configuration shown in Figure 9(b) with parameters in Table III.

TABLE III: Initial and Final Orbit Sizes with Respect to the Mothership of Each Ring

Ring	Color (Fig. 9)	Initial Configuration		Final Configuration	
		Semi-Major Axis (km)	Inclination (deg)	Semi-Major Axis (km)	Inclination (deg)
1	purple	200	0.0	400	0.0
2	green	160	25.5	300	18.5
3	blue	140	150.0	200	138.0
4	cyan	100	45.0	100	63.5

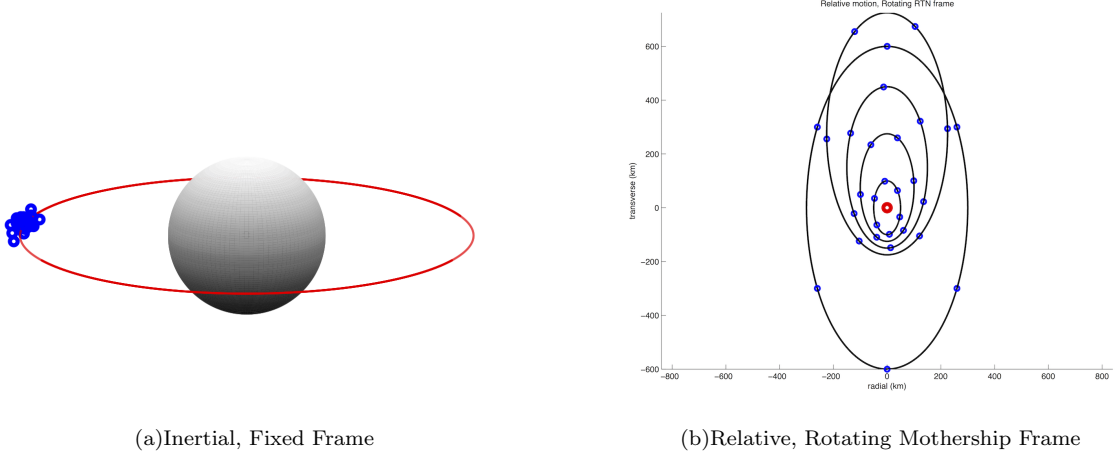


FIG. 8: Orbit design for mothership and daughterships in inertial and relative frame. The orbits of the daughterships are termed “rings.”

C. Coverage and Baseline Computations

The formation design is driven by adequate coverage of collection targets, with coverage defined by the diversity of baselines formed by individual daughtership pairs. A single baseline is the projection of the relative position vector from one daughtership to another, into the plane perpendicular to the direction to a target. Baselines are computed beginning with the relative position vector from daughtership i to daughtership j , $\vec{\rho}_{ij}$, and the unit vector to a target, \hat{e}_\star . Both vectors are assumed to be in a common inertial frame, EME2000 for this study. First, a new frame for projecting the position vectors is formed using the target vector and the z-axis unit vector in the EME2000 frame:

$$\begin{aligned}\hat{e}_z &= \hat{e}_\star \\ \hat{e}_y &= \hat{k} \times \hat{e}_z \\ \hat{e}_x &= \hat{e}_y \times \hat{e}_z\end{aligned}$$

where \hat{e}_x , \hat{e}_y , and \hat{e}_z are the unit vectors defining the target frame; and \hat{k} is the unit vector in the EME2000 z direction. For targets near 90° declination, the EME2000 x direction can be used in place of the z direction. With this target frame constructed each position vector $\vec{\rho}_{ij}$ is projected into the xy -plane of the target frame to yield (r, θ) pairs describing the baseline:

$$\begin{aligned}r &= \sqrt{b_x^2 + b_y^2} \\ \theta &= \tan^{-1}(b_y/b_x)\end{aligned}$$

where b_x and b_y are the components of $\vec{\rho}_{ij}$ in the x and y directions of the target frame, respectively ($b_x = \vec{\rho}_{ij} \cdot \hat{e}_x$ and $b_y = \vec{\rho}_{ij} \cdot \hat{e}_y$). We operate with (r, θ) terms instead of usual u, v components for convenience given the geometry of the problem. When computing baselines it does not make a difference if the baseline is measured from daughtership i to j , or vice-versa. Because of this a baseline of (r, θ) counts the same as one in the opposite direction, $(r, \theta + 180^\circ)$, and a formation of n daughterships will have $n(n-1)/2$ unique baselines at a given sample time. For the purpose of computing coverage the (r, θ) space is divided up into N bins in the r direction and M bins spanning 180° in the θ direction, and credit is taken for each bin covered by a baseline. As the formation orbits the Moon and formation geometry changes, new baseline measurements are taken, and the overall coverage consists of the different (r, θ) bins which have been collected. If N_{collect} is the number of bins collected over some period of time then a numerical coverage score, J , can be computed from $J = N_{\text{collect}}/(NM)$.

Figures 10 and 11 show uv -plane coverage for the formation in the initial configuration in Table III, against two different targets in different directions. The different coverages obtained reflect the assumed target source declinations, and the resulting differences in collection geometry. As the mothership orbit lies in the EME2000 xy -plane, the cumulative baseline pattern will be flatter against targets with low declinations; the pattern will be more round against targets with high declinations. What thickness exists in the coverage pattern against low-declination targets

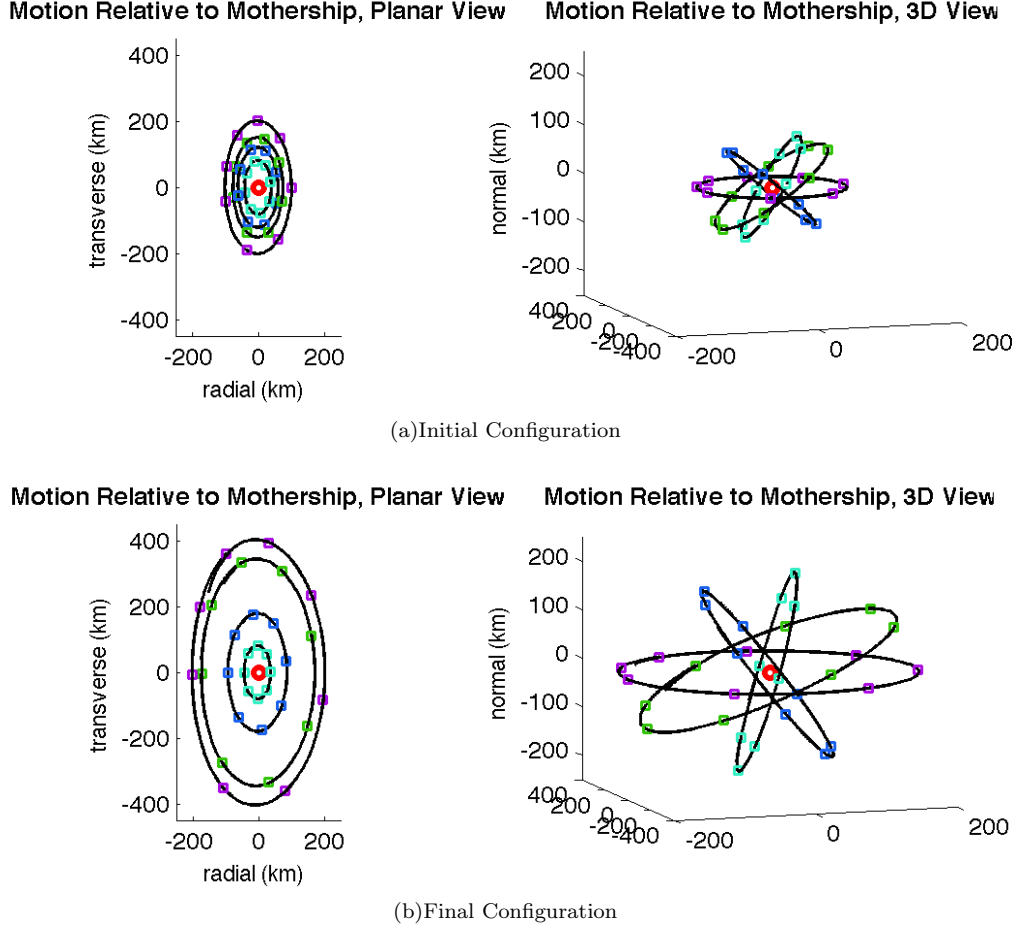


FIG. 9: Reconfiguration of the daughterships from their initial configuration to the final configuration. In all panels, the configurations are shown in a relative, rotating frame fixed at the mothership, which is represented by the red dot at the origin.

is due to the out-of-plane components of the outer rings. Once the final configuration is achieved, the coverage pattern will cover a greater area.

D. Communications and Data Downlink

1. RELIC Communications Architecture Definition

Figure 12 illustrates a few examples of the topologies derived from our communications trade analysis. The daughtership-to-daughtership mesh is primarily used for ranging, discussed further below. Direct-to-Earth (DTE) daughtership communications were considered for a mission concept that would not include a mothership, but the communication demands on a small spacecraft, for the required data rates, were judged infeasible. In general, the communications architecture and its requirements were based on the traffic loads, the spatial distribution and dynamics of the daughterships, and onboard science data compression processing.

In conjunction with topology selection, we conducted a study on different radio frequency bands (UHF, S band, X band, Ka band) together with alternative antenna types (dipoles, parabolic, patch) and transmit power levels. Figure 13 shows an example for a daughtership-to-mothership communications link using a UHF half-wave dipole. Assuming each daughtership transfers its science data directly to the centrally-located mothership, the radio range constrains the spatial extent of the constellation, which in turn impacts the resolution capability of the science array. Systems engineering considerations such as cost and feasibility of deploying different antenna types on cubesat-class daughterships also had a significant influence on forming the resulting communications architecture.

Assuming a phased concept of operations, we found that the duration required to crosslink the science data from

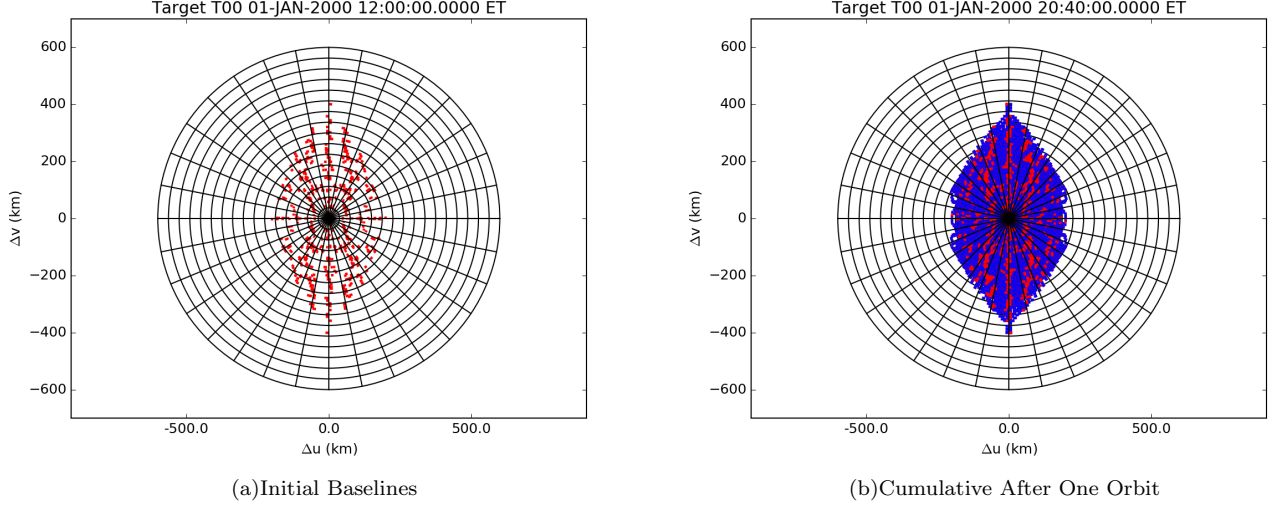


FIG. 10: The uv-plane coverage for the initial configuration of daughterships. In this example, the target radio galaxy is at considered to be at a right ascension of 0° and declination of 0° ; similar coverage diagrams apply for sources at comparable declinations. A total of 128 bins in the radial direction and 128 bins to cover 180° in θ , with gridlines every 8 bins. This number of bins seems to be optimal for up to $30'$ size of the radio galaxy. Red bins indicate the instantaneous baselines at the time given while blue bins show bins already collected, with samples taken every 10 minutes. The left panel shows the initial set of baselines collected while the right panel illustrates the cumulative baselines acquired after one orbit period.

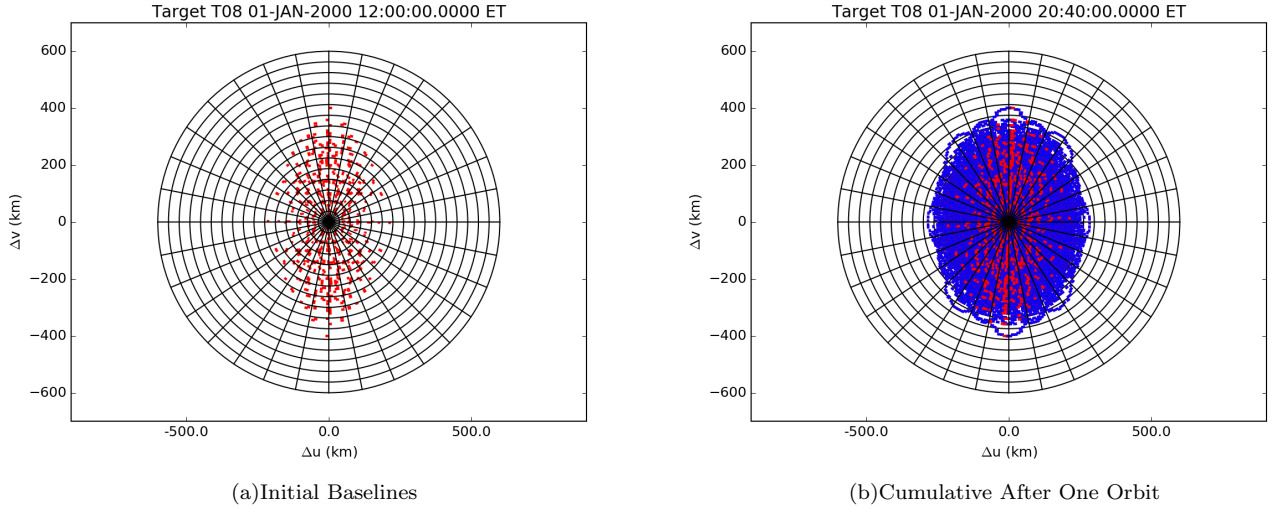


FIG. 11: The uv-plane coverage for the initial configuration of daughterships. In this example, the target radio galaxy is at considered to be at a right ascension of 0° and declination of 45° ; similar coverage diagrams apply for sources at comparable declinations. A total of 128 bins in the radial direction and 128 bins to cover 180° in θ , with gridlines every 8 bins. Red bins indicate the instantaneous baselines at the time given while blue bins show bins already collected, with samples taken every 10 minutes. The left panel shows the initial set of baselines collected while the right panel illustrates the cumulative baselines acquired after one orbit period.

the daughterships to the mothership dominates the proportion of total mission operations (Figure 6). The baseline method to transfer daughtership science to the mothership consists of a series of scheduled daughtership-to-mothership crosslinks until all data is collected at the mothership; this is essentially a coarse Time Division Multiple Access (TDMA) approach. One possibility to reduce the total time required for this phase is to use Frequency Division Multiple Access (FDMA). In this case, the mothership has the enhanced capability to receive multiple crosslink channels simultaneously. For cost and scalability, each daughtership is a smallsat having limited resource capabilities,

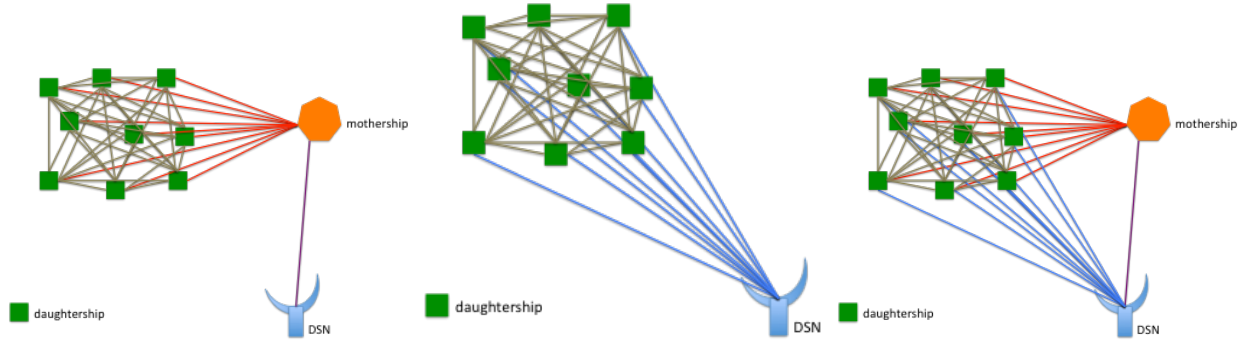


FIG. 12: Potential constellation communications topologies for a space-based radio astronomy array. For clarity, the mothership (orange) is shown spatial offset from the center of the constellation, but, in the actual design, it would be located near the center in order to minimize the communication range.

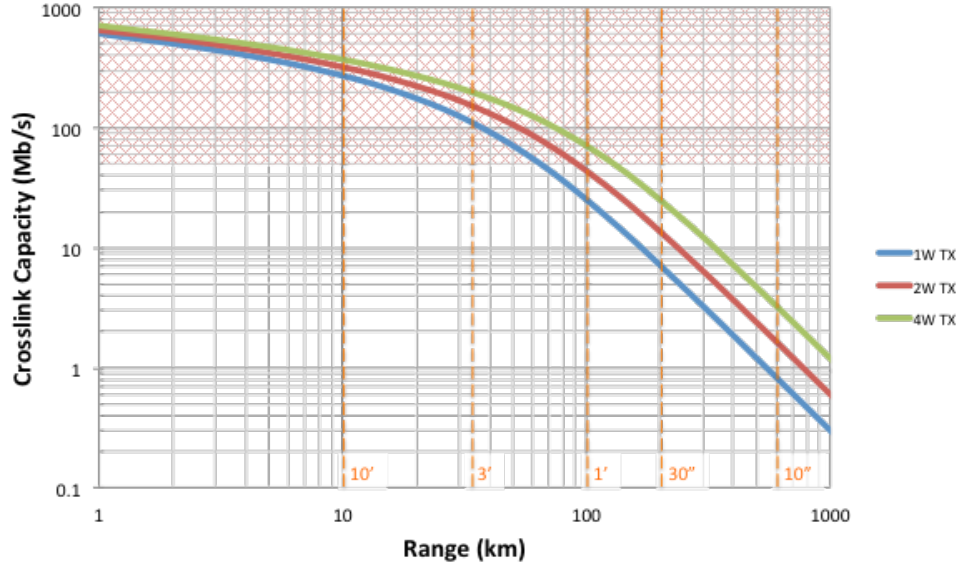


FIG. 13: Daughtership-to-Mothership crosslink communications data rate vs. range using UHF $\frac{1}{2}$ -wave dipole antennas. Vertical lines indicate angular resolution for science array at different constellation spatial radii.

which is maintained by the FDMA approach that imposes greater capability only on the mothership. According to our operations concept, crosslink transfers will be scheduled to occur when the daughtership-mothership range is small in order to achieve maximum data rate capacity. Because the daughterships are in motion, each daughtership radio must be able to re-tune its FDMA channel, since the set of daughterships in close range is dynamic (this is a very modest requirement). Some technology development would be required to enable the mothership multi-receive capability, but it would be possible to implement a multi-user modem in an architecture developed by [56]. It is also noted that sufficient spectral bandwidth will need to be allocated to accommodate the multiple crosslink frequency bands. We also conducted an analysis to determine the potential benefit of using multi-hop communications among the daughterships to transport science data to the mothership. That is, rather than a daughtership transferring its science data directly to the mothership, it may be advantageous to transfer it to another daughtership which will then relay it to the mothership (possibly via even more daughterships). The potential benefit depends on the spatial distribution of the nodes, and arises from link performance being directly proportional to the square of the distance (in free space).

We take the approach of assuming each daughtership transmits at a fixed power but is able to adjust its data rate so as to meet a specified link margin. For example, denoting r_{ij} as the distance from daughtership i to daughtership j and r_{jM} as the distance from daughtership j to the mothership, then it will take less time to transfer the science data from daughtership i via daughtership j whenever $r_{ij}^2 + r_{jM}^2 < r_{iM}^2$. Based on this model, we determined improvements from using multi-hop routing by analyzing the spatial distribution of nodes at different snapshots of mission time,

assuming a reasonable choice for the daughtership orbits. Table IV presents results found.

TABLE IV: Multi-hop Gains at Different Mission Times.

Days into the mission	max range from mom (km)	max internode range (km)	# of 2- or 3-hop paths <1-hop	2-hop time reduction	# of 3-hop paths <1-hop	2- or 3-hop time reduction
15 days	260.23	492.10	16	22.3%	2	22.9%
30 days	297.91	583.41	18	27.7%	4	31.9%
40 days	341.08	700.04	23	31.5%	6	36.7%
54 days	402.67	782.33	19	27.3%	4	30.0%
mean	325.47	639.47	19.0	27.2%	4.0	30.4%

The maximum range to the mothership and between any nodes is included for a general sense of constellation span. A mean of 19 of the 31 daughtership-to-mothership paths are improved by multi-hop, 4 of which are 3-hop paths. No cases of 4-hop paths were found to provide benefit. The reduction in time to transfer all data is reduced by mean of 30.4. An indication of the routing paths is depicted in Figure 14. This corresponds to day 40 of the mission. A planar projection is shown, and thus link lengths may appear somewhat contorted. We see that certain intermediate nodes are selected to relay data on behalf of numerous “outer” constellation nodes.

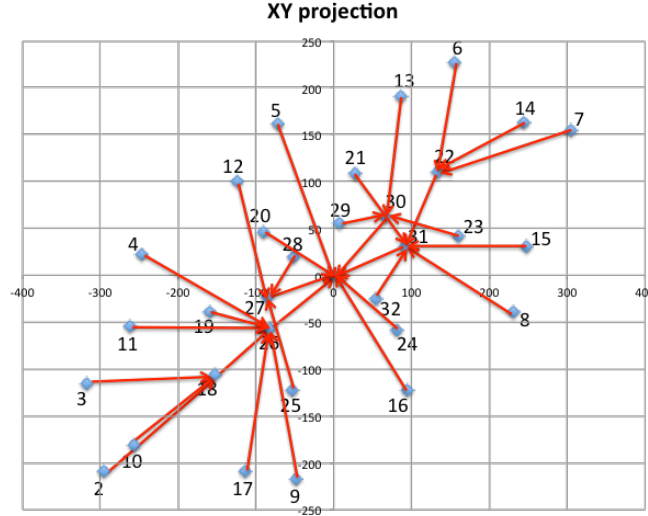


FIG. 14: Multihop paths to mothership, 40-day case.

Practical considerations of using multihop communications include the following:

1. Daughterships will need to communicate with one another at the “return telemetry” data rate. Space radios typically operate using full duplex (i.e., different channels for transmission and reception) with different possible rates in each direction. (Typically “command” data rate is much less than the “telemetry” data rate.) Even if the rates are symmetric, coordination of the inbound/outbound channels will be necessary. An alternative is to use half-duplex (single-channel) communications, but full duplex is typically used to support ranging and Doppler measurements. It is noted that full duplex may allow simultaneous reception (of data to be forwarded) and transmission, which would further speed the transport of data, however the analysis above did not assume this.
2. Selectable data rates will be constrained to some number of specific discrete values, and this quantization will yield some degradation of the results shown above.
3. There will be more energy consumed for daughtership relay receptions.
4. Certain “inner” daughterships will bear the burden of relaying data from numerous “outer” daughterships, in addition to its own science data, so that the work is unevenly distributed.

5. One might consider orbit selection that also accounts for improved multihop performance; currently we have focused primarily on science quality.

E. Data rate discussion

We considered the following options for the data downlink:

- raw waveform downlink
- using polyphase filters
- Fast Fourier Transform, FFT, on board
- 1, 3 and 12 bit signal digitization, N_{dig} .

We also assume 2:1 lossless compression ratio in addition to any data reduction technique used. For this discussion, we only consider the transmission at the carrier frequency. The data rate for each case is described below.

1. Raw data downlink

The raw data downlink assumes that the recorded waveform is transferred to the mothership continuously. In the calculations below, we assume the highest frequency of the system to be 30 MHz, requiring $f_N = 60$ MSps digitization speed. For a 1-bit digitization, the resulting data rate is 60 Mbps per daughtership for two polarizations. We assume a factor of 2 lossless compression of the signal. The data transfer rate grows linearly with the digitization depth, and, for 12-bit digitization, equals 720 Mbps. An array of 32 daughterships would require about 24 Gbps downlink.

2. Polyphase Filters

The basic idea of polyphase filters is the splitting of the channel into multiple narrow band channels with subsequent digital heterodyning of each channel. For instance, a 16 kHz wide channel would require only 32 kSps digitization speed. The narrow-band channels are later combined reconstructing the original signal with minimal loss. More details on the subject can be found in [57].

The use of polyphase filters allows to reduce the data rate by a factor of 60; in the case of 12-bit digitization, the data would be about 12 Mbps per daughtership or about 384 Mbps for the whole 32-daughtership constellation.

3. FFT Onboard the Spacecraft

The idea is to do fast Fourier transform of the recorded waveforms, FFT, on board the individual daughtership and downlink the FFTs instead of the raw waveforms in order to perform the cross-correlation either on board the mothership or on the ground. This approach would reduce substantially the data rate required.

If the number of required frequency samples in the FFT, N_{freq} , is taken to be 64 and if N_{time} is the number of samples in the time domain, then the FFT would have to have $\frac{1}{2}N_{time}$ samples. In order to obtain N_{freq} , a minimum $N_{time} = 128$ samples would be required; for the purpose of averaging, the next higher number should be used, which would be 256 in this case.

The minimum integration time required to obtain N_{freq} is $t_{int} = \frac{N_{time}}{f_N} = \frac{128}{60 \times 10^6} \approx 2 \times 10^{-6}$ s. We cannot have integration time less than this value if we aim to obtain at least 64 samples in frequency domain. Assuming continuous observation, the downlink data rate is $R = N_{freq} \times \frac{N_{bits}}{t_{int}} \approx 350$ Mbps, or 11 Gbps for an array of 32 daughterships, assuming 2:1 lossless compressing offsetting two polarization signals per daughtership. The data rate calculated above represents a lower limit of the integration time. The usual internal integration time of the receivers is about 1 s, meaning the real data rate will be about 6 orders of magnitude lower and the minimal integration time condition fulfilled without any problem.

F. Ranging system requirements

In order to provide initial condition for science data processing and radiometrics for orbit determination, position knowledge and time derivatives must be obtained for each daughtership. We discuss the effect of the time derivatives in Section V and only consider the baseline vectors here. In order to reduce cost and improve operational scalability, position knowledge is derived from a two-tiered process. On the top tier is the mothership, for which the absolute position is determined by standard DSN procedures. At the second tier, the relative position of each daughtership to the mothership is derived from a combination of gravity model and crosslink range measurements performed within the constellation.

The desired upper bound on position knowledge uncertainty is 30 m, roughly equal to the wavelength at 10 MHz. Assuming that each daughtership's relative position can be computed through multi-lateration of range estimates with one-third of the constellation nodes, i.e., 10 other daughterships, simulation shows that a range estimation error no greater than 1 m is desired. In terms of navigation, the minimum safe separation distance is 3 km, which is much larger than the 30 m science requirement that will form the basis of our ranging system design and analysis. Due to daughtership motion and expansion of the constellation orbits, it is estimated that at a minimum inter-spacecraft range should be measured every 10 to 15 minutes. Although there are 496 unique bi-directional inter-daughtership crosslinks at any given time, in order to derive sufficient position knowledge, we expect that each daughtership will need to range with approximately 10 other daughterships, reducing the number of measurements below the worst case of 320—the exact number required depends on the geometry and how many redundant measurements can be eliminated, as the range estimate from daughtership i to j is symmetric with daughtership j to i . Assuming an integration time of 1 s for each measurement, it takes 320 s to complete one cycle of ranging measurement. In reality, it will take much less than that time since ranging measurements with sufficient spatial separation can be conducted simultaneously.

1. Strawman Design of Crosslink Ranging System

In designing a crosslink ranging system, we attempt to maximize dual-use of the relay communications system's transceiver and antenna to save cost, weight, and most importantly space on the daughtership. Currently we assume that the mothership will utilize the same relay system as the daughtership although it is definitely possible for the mothership to carry a compatible yet far more capable system in flight. For our strawman design, however, we assume that the relay system is identical on both the mothership and the daughterships. We assume that the relay system may operate around 500 MHz (UHF) or 8.4 GHz (X-band). For UHF operation, we consider a single dipole antenna extending along the Z axis at half-wavelength or $\frac{5}{4}$ wavelength, the latter having higher directivity but narrower beamwidth. For X-band operation, four pairs of transmit and receive patch antennas mounted on the four sides of the daughtership, facing the $+X$, $-X$, $+Y$ and $-Y$ axis directions, provide higher gain than dipole and wide coverage. We consider these two antenna initially to minimize pointing requirements. As we will describe later, a horn antenna option was also considered with increasing operational complexity due to pointing requirements.

In terms of ranging technique, we consider PN ranging using either coherent (turn-around) mode or regenerative mode. Sequential tone ranging require synthesizing different carrier and good knowledge of starting time, both are difficult to implement within a constellation of smallsat. Therefore, only PN ranging is considered in our study. Coherent mode has the advantage of eliminating frequency mismatch between the uplink and the downlink at the cost of requiring a transponder, while regenerative (non-coherent) mode achieves better economy by using a transceiver and provides some degree of performance advantage under high noise environment. As the relay system design trade is still open, both coherent and non-coherent modes are considered in our analysis. To analyze ranging system performance, we used two PN codes [58], one designed for coherent and the other for non-coherent ranging, and assume a nominal ranging clock of 1 MHz. For turn-around ranging, the noise equivalent bandwidth is 1.5 MHz. Since both codes have an ambiguity resolution of 75,660 km [58], far greater than the size of the constellation orbit with maximum baseline of 600 km, they are suitable for our purpose.

We assume that the ranging signal will utilize squarewave, and the transponder's automatic gain control (AGC) delivers constant root-mean-square (RMS) voltage. We do not consider the more complex scenario of simultaneously ranging and carrying command and telemetry on the crosslinks, therefore all transmit power is allocated to the ranging signal component. Although under good SNR environment there is no reason not to exchange command and telemetry while ranging and there is good potential for reducing latency, it is the beyond the scope of this initial analysis.

The root-mean-square error of the ranging measurement is given by [58]

$$\sigma = \frac{c}{\sqrt{f_{RC} A_C R_1 \sqrt{256 T \frac{P_R}{N_0} |_{D/L}}}}, \quad (1)$$

where f_{RC} is the frequency of the range clock, A_C is the fractional loss of correlation due to frequency mismatch (0 for coherent mode with assuming Doppler rate aiding [59]; $|\sin c(2f_{RC}T)|$ for regenerative mode, where f_{RC} depends on oscillator accuracy and stability, with no Doppler rate aiding assumed), R_1 is cross-correlation factors for the PN code, T is the integration time (in seconds), and $\frac{P_R}{N_0} |_{D/L}$ is the ranging signal signal-to-noise ratio on the downlink. For turn-around ranging, the uplink noise has a much higher contribution to the downlink signal-to-noise ratio than regenerative ranging. A detailed description of the relationship between the uplink and downlink SNRs and their respective contribution to the ranging error can be found in [58]. Table ?? summarizes the required $\frac{P_R}{N_0}$ for achieving 1 m accuracy, as derived from equation 1.

TABLE V: Crosslink Ranging Accuracy and SNR Requirements.^a

Ranging Technique	Received Pwr (uplink, W)	Required $\frac{P_R}{N_0}$ (downlink)	Ranging Accuracy (m, RMSE)	Integr. Time (s)	Antenna Type
Turn-around (UHF)	1.09×10^{-14}	1.05×10^6	0.05 0.016 0.006	1 10 100	$\frac{1}{2}$ wave dipole, 2.1 dBi 1.25 wave dipole, 5.1 dBi
Regenerate, non-coherent (UHF)	1.09×10^{-14}	2.13×10^6	0.25 0.23	1 2	$\frac{1}{2}$ wave dipole, 2.1 dBi 1.25 wave dipole, 5.1 dBi
Turn-around (X-band)	1.30×10^{-15}	4.82×10^2	1	6	conical hornm 11 cm aperture, 17.07 dBi
Regenerate, non-coherent (X-band)	1.36×10^{-16}	2.90×10^4	1.45	1	patch (1.4×1.1 cm), 7.2 dBi

^aPatch antenna parameters: dielectric constant of substrate = 2.2, height of substrate is 0.16 cm, width is 1.41 cm, length is 1.1 cm, resonant frequency is 8.4 GHz

Table V shows that to achieve 1 m accuracy, 1 sec integration time will be sufficient except in the case of the X-band turn-around ranging, where a horn antenna and more accurate pointing will be required. The next step in our analysis is to apply the required $\frac{P_R}{N_0}$ threshold when simulating the orbital geometry and antenna pointing in order to collect statistics on ranging opportunities in the natural course of a two-month long observation campaign.

2. Constellation Ranging System Performance Analysis

We utilized binary SPK kernels developed during the orbital design and generated daughtership orientation kernels that help model pointing and compute antenna and received power levels. Due to the constant motion and the need for orbit maintenance, we assume that ranging could occur during both science collection and data relay phases. For the initial two-month long scenario, we assume for sake of simplicity that the primary orientation for all daughterships is to have the $+Z$ axis pointed in the direction normal to the orbital plane of the mothership, and that for the secondary orientation the $+X$ axis is pointed toward the Sun to maximize power generation. In reality, we expect the constellation network pointing to be different depending on whether it is optimized for science or relay. However, we make this simplifying assumption in order to quantify, at a coarse grain level, the temporal characteristics of the ranging links.

This model incorporating the daughtership trajectory, orientation, antenna radiation pattern, and ranging link analysis is used to simulation the geometry and ranging performance of the constellation network. Figure 15 is a screen shot of some of the metrics generated by the simulation such as the antenna pattern, the crosslink range and range rate, the received signal power, and the feasible ranging links meeting certain SNR threshold. In our simulation study, we assume a transmit power of 4 watts, Allen deviation of the oscillator to be 1×10^{-9} Hz/s, and noise temperature of 290K + 50K of cosmic background. The simulation focused on three configurations: (a) UHF band turn-around ranging with half-wavelength dipole, (b) UHF band turn-around ranging with 1.25 wavelength

[69] Patch antenna parameters: dielectric constant of substrate = 2.2, height of substrate is 0.16 cm, width is 1.41 cm, length is 1.1 cm, resonant frequency is 8.4 GHz

dipole, and (c) X-band regenerative ranging with 4 pairs of patch antenna. For dipoles we use computed antenna patterns in our model; for patch antenna, we use a “cookie-cutter” model in which half the maximum antenna gain is assumed when a target is within the 3dB beamwidth and all targets outside the beamwidth are assume unreachable. Those configurations not covered by our simulations, namely, UHF with regenerative ranging and X-band turn-around ranging, are still open options to be considered in future studies.

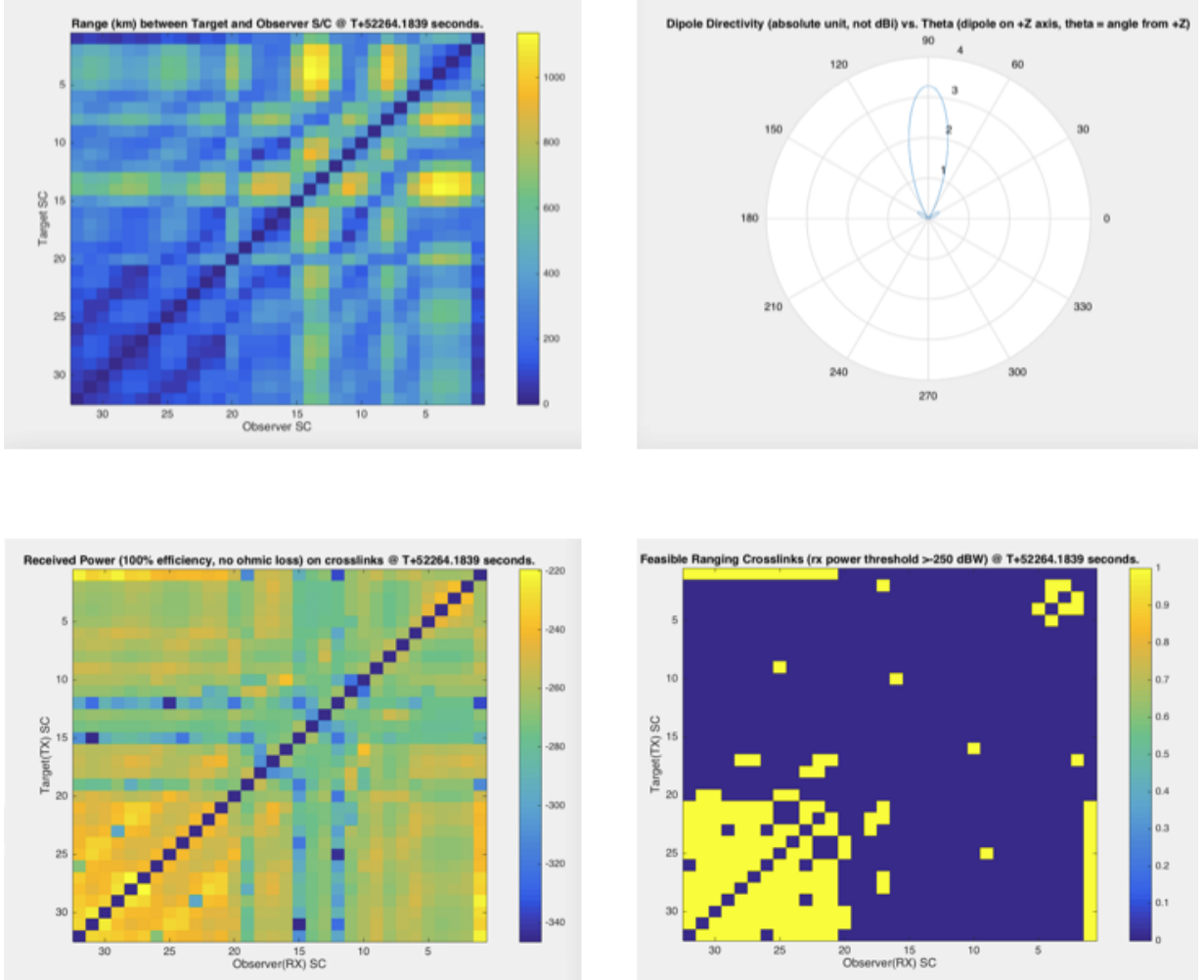


FIG. 15: An example of constellation crosslink geometry simulation. Upper left: Range between the target and the observer. Upper right: dipole directivity used for the simulation. Lower left: power received assuming 100% efficiency. Lower right: feasible ranging cross-links assuming 250 dBW power threshold.

Figure 16 shows the histogram of the fraction of all crosslinks that is able to achieve 1m accuracy. The simulation covers 15,438 5-minute time steps, approximately 54 days of operation. At each time step, the ranging signal SNR is computed for all possible crosslinks, taking into account antenna pointing, radiation pattern, and space loss, and the percentage of crosslinks that can achieve 1m accuracy is recorded in the histogram. The result shows that our baseline constellation geometry achieves excellent ranging coverage for all three configurations considered. The half-wavelength dipole at UHF has the best coverage such that at all times more than 90% of all crosslinks can deliver 1m accuracy ranging. Upgrading to the 1.25 wavelength dipole provides 3dB increase on antenna directivity but reduces the number of feasible ranging links to an average of 70%. For X-band using 4 pairs patches, on average more than 60% of the crosslinks are feasible for conducting ranging measurements.

In order to better understand how many ranging measurement can be done per daughtership with a short time window, we need to further analyze the distribution of the feasible ranging links among the 32 daughterships. Figure 17 shows the mean and standard deviation of the number of feasible ranging crosslinks for each daughtership sampled over 15,438 time instances. The same general trend persists, whereby the half-wavelength dipole achieves the highest average number of feasible ranging links and lowest standard deviation. As might be expected, the ranging opportunity would be better for those daughterships in the inner rings (daughterships 1 to 9) than those on the outer rings. For

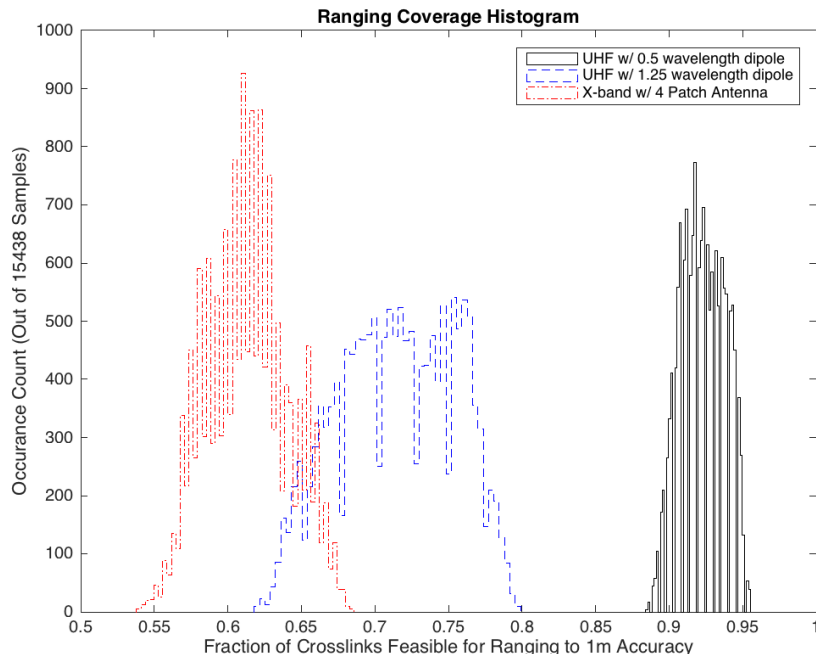


FIG. 16: Histogram of the Fraction of All Crosslinks Achieving 1m Ranging Accuracy Per Time Instance

the worst case, the outer ring with X-band crosslinks, there would be an average of 15 feasible ranging links per daughtership, with a standard deviation of 4, which would be acceptable. Even for daughterships in the outer ring, it is not difficult to achieve 30 m position knowledge. Given the short integration time of only 1 s, we do not anticipate that there would be difficulty in providing timely ranging estimate updates to support both science processing and orbit maintenance.

One of the outstanding issues that has not been adequately addressed in our preliminary study is interference avoidance while ranging. Further analysis is required to determine the required spatial and angular separation when several crosslinks conduct ranging operations simultaneously. In that context, the benefit of implementing FDMA or 802.11-like CSMA medium access control (MAC) protocols for coordinating the crosslink communications and ranging can also be evaluated. As the mission concept is further refined, it should become possible to incorporate a more detailed daughtership orientation profile into the ranging simulation. Along that same line of investigation, a more detailed trade study between using high gain antenna and its effect on pointing and scheduling of science, relay, and ranging operations. Finally, there is the concept of simultaneous command/telemetry transmission and ranging; the potential saving in latency and power should be quantified in terms of impact on ranging accuracy. Recent advanced in telemetry-based two-way ranging [60] research shows great potential in reducing range jitter by taking advantage of high rate telemetry signal structure. These advancements in ranging research should be also incorporated into future studies.

IV. STRAWMAN SPACECRAFT

In order to form an interferometer, all of the signals from the individual antennas must be brought together for *correlation*. In ground-based telescopes, the correlation occurs in a dedicated processing centers. For the RELIC design, we have retained this architecture, which necessitates a mothership to which daughterships send the collected science signals. Because of their different functions, the daughterships and the mothership cannot be identical, and we describe each in turn. Our focus is on the daughterships, as key elements of the telescope—the reception of radio waves and the position determination—are associated with the daughterships, while the mothership design is more straightforward.

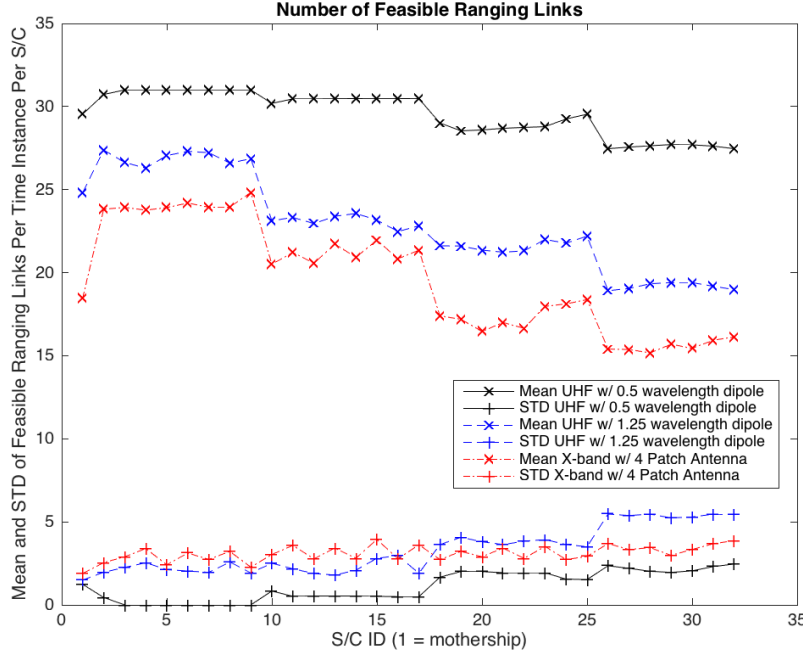


FIG. 17: Number of Feasible Ranging Links per Daughtership per Time Instance.

A. Daughtership Design

As described above, the required effective aperture exceeds 100 km leading us to adopt an interferometric design for the RELIC mission. This design choice allows us to leverage a significant knowledge base [61] and experience from ground-based interferometric telescopes, including many that operate at frequencies not too dissimilar than those of RELIC [19–26].

A natural approach to an interferometric telescope is for it to consider of a number of identical daughtership spacecraft, with each daughtership carrying a single science payload consisting of an antenna and receiver. This approach is what has been adopted in previous mission concepts [e.g., 27, 28, 31–33], and it is a straightforward extension of how ground-based interferometers are designed. The science payload itself is relatively simple, the daughtership would be exposed to essentially identical environmental conditions allowing them to be identical, and the design can leverage economies of scale in constructing multiple identical spacecraft.

The daughterships are designed to conform to a 6U form factor (10 cm × 20 cm × 30 cm) as the science payload itself is not large and this form factor allows significant leveraging of compact and standard components, thereby likely minimizing overall mission cost. Table VI summarizes key high-level parameters of the daughtership design, and Figure IV A presents the physical layout of a daughtership. The remainder of this section presents details of specific sub-systems within a daughtership.

The daughterships would be deployed from a container (“pod”), which secures the daughterships during launch and transportation to the final orbit. The “pod” also would provide initial momentum for reaching the desired orbital configuration.

1. Science Payload Subsystem

The science payload consists of a dual-polarized antenna, receiver, and associated signal processing unit capable of receiving radio frequencies between 0.1 MHz and 30 MHz. Following standard practice, we adopt an electrically short dipole, as the system temperature is determined entirely by the synchrotron emission of the Galaxy [9] and dipoles approaching resonance are large enough to be potentially mechanically unstable [18].

For this design, a motorized, deployable dual dipole antenna has been chosen. Dipole antennas have been developed that, when stowed, can fit within a volume of 0.5U and, upon deployment, have an effective length for each of the four poles of 1.2 m. More details about the antenna design are provided in Appendix A.

TABLE VI: Daughtership Parameters

Property	Value (Incl. Contingency)
Mass	< 14 kg
Peak Power Consumption	52 W
On-Board Data Storage Capacity	32 GB
Form Factor	6U (10 cm × 20 cm × 30 cm)
Pointing Accuracy	< 0.03°
Slew Rate	10°/s
Maximum Thrust	> 1 N
Available ΔV	> 100 m s ⁻¹
Maximum Power Generation (beginning of life)	62.5 W
Battery Capacity	77 W hr
Expected Unit Cost (incl. payload)	\$5M (TBC)

The receiver and signal processing unit amplify, condition, and sample the incident radio waves. Designs for such units are well developed [e.g., 13–16]. For ground-based systems, analog signals are digitized with anywhere from 1 bit to 24 bits per sample. For a space-based array such as RELIC, data transmission is a significant factor and high bit depths can lead to infeasible data rates. We have baselined 12 bits per sample to enable sufficient bit depth to handle the range of powers expected over the relevant frequency range. We further employ a polyphase filter bank to produce a set of frequency sub-bands [63] The resulting effective data rate for science data collection is 12 Mb s⁻¹ per daughtership.

The overall power usage of the science payload subsystem is expected to be less than 10 W in operation and less than 1 W when the device is in standby.

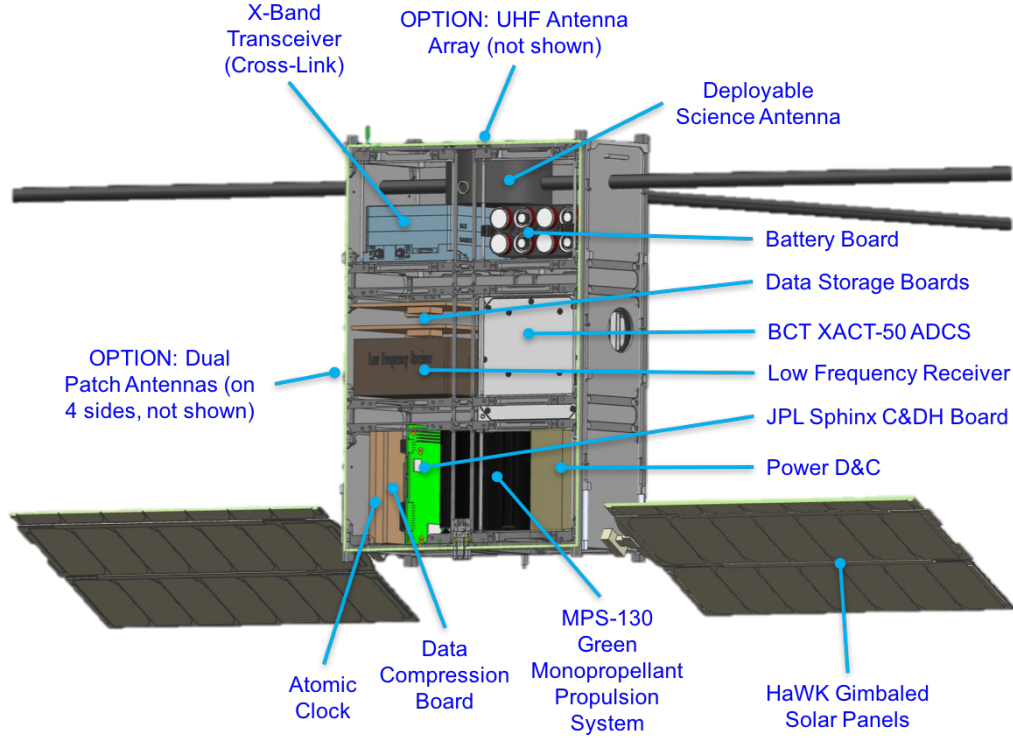


FIG. 18: Physical layout of the RELIC daughtership spacecraft. Cabling is not shown.

2. Communications Subsystem

The communication subsystem is required not only to transmit data from the daughterships to the mothership but also to conduct ranging between neighboring daughterships in order to determine relative positions for the interferometry. A key trade for the communications subsystem is to minimize the power required while maximizing the data rate.

Two, nearly equivalent options exist for the communications subsystem. Option 1 is an ultra-high frequency (UHF) system operating at 450 MHz, using a deployable, canted turnstile antenna with a gain of 1 dBi at 450 MHz and with an operational frequency range of 400 MHz–480 MHz. Option 2 is an X-band system operating at 8.5 GHz. For this design, a set of four pairs of high-gain patch antennas tuned to 7.4 GHz (receive) and 8.5 GHz (transmit) and a gain of 12 dBi, each mounted to a 10 cm \times 10 cm surface on four sides of the daughtership was selected.

Both options use approximately 5 W of power to transmit the required data rates. The X-band option is based on marginally less mature technology for small spacecraft, but it brings the advantage over UHF of being more compact and carrying less risk of possible interference with the science payload. Conversely, the UHF option is likely to be less costly and less complex (particularly since only one antenna array is required).

In order to allow for sufficient link margin, design parameters of a 16 Mbps at 100 km distance from the mothership were used.

One potential complication is that requirements on allowable frequencies for inter-satellite links in lunar orbits may not be satisfied using either X- or UHF-band solutions. A waiver may be required to implement either of these options.

3. Command and Data Handling Subsystem

Each daughtership has a command and data handling (C&DH) subsystem, consisting of a data processing unit and data storage. The requirements on the data processing unit are modest, in that the flight computer is primarily to be used for navigation and ranging. Data storage is primarily to be used for buffering data to be downlinked.

As an initial design for RELIC, the radiation-tolerant flight computer Sphinx, developed at JPL, was selected. The Sphinx fits within the allowed 6U form factor and features a reprogrammable field programmable gate array (FPGA) and a Leon3 dual core processor clocked at 100 MHz. The Sphinx flight computer board has 8 GB of radiation tolerant (192 krad total dose) non-volatile memory, and features a number of interfaces, including a high-speed dual SpaceWire adapter capable of supporting up to 200 Mb s⁻¹. The latter is required during the cross-link phase to forward communication packets to the communication subsystem at desired speeds.

Data collected by the science payload on the daughterships could not be cross-linked to the mothership simultaneously, particularly due to the large number of daughterships. Therefore, a buffer is required. The amount of memory on the Sphinx flight computer is not sufficient to store the data from a typical RELIC observation (4 hr generating 22 GB). Allowing for additional spacecraft housekeeping data, error correction checksums, and contingency, a total of 32 GB is needed. This data storage volume is met by using four 8 GB memory modules (e.g., radiation tolerant FLASH NAND). An appropriate board housing these memory chips, and providing an appropriate high-speed data interface and controller do not yet exist and would need to be designed.

4. Attitude Determination and Control Subsystem

In order to orient the daughterships to conduct the science observations and for power generation for the solar panels, the daughterships are equipped with an attitude determination and control subsystem (ADCS). Requirements with respect to pointing accuracy for the science observations are modest, estimated to be 0.1°, given the large power patterns provided by the electrically short dipoles.

Required for the RELIC daughterships are at least three reaction wheels for 3-axis control, an equal number of torque rods to decrease Δv requirements for desaturation, and star trackers for positional determination. A plethora of off-the-shelf components for ADCS exist that would meet the requirements.

5. Propulsion Subsystem

The mission concept of operations specifies a number of maneuvers that require a propulsion system. These maneuvers are initial configuration of the constellation, from drop-off from the transfer vehicle to the initial formation; regular station keeping; and reconfiguration maneuvers that increase the number of baselines. A 3-axis propulsive

control system is required for desaturation of the reaction wheels due to the long mission duration. Table VII summarizes these different propulsion requirements, as currently understood.

TABLE VII: Maneuvers and Corresponding Required Δv

Maneuver	Required Δv (m/s)
Initial Configuration	20
Reconfiguration (20 [TBR] times)	1 (per reconfiguration)
Station Keeping	< 1 (per day) (TBR)
Desaturation	TBD

There are a number of types of propulsion systems available for small spacecraft, which can be classified broadly into chemical (cold vs. warm gas, mono- vs. bi-propellant.), electrical (ion, Hall-effect), and propellantless (solar sail.) drives. Propellantless and electrical drives have very low maturity and produce little thrust. Cold and warm gas drives have low energy density fuels, requiring large quantities to satisfy the Δv requirements. A number of mono- and bi-propellant drives exist, capable of providing upto 100 m s^{-1} of total Δv , 3-axis control, and not requiring toxic fuel (thereby avoiding the need for a waiver).

6. Power Subsystem

Due to the desired high data rates and required data volume, power requirements are higher than is typical for small spacecraft. Table VIII summarizes the mission profile, which is illustrated in Figure IV A 6, that was used in order to design the electrical power system (EPS), including determining the size of the solar panels and batteries. Most power modes assume a number of instruments being on (including heaters), and each power mode assumes a 30% contingency.

TABLE VIII: Primary Mission Power Modes and Durations

Mode				Propulsive Maneuver	
	Cruise / Idle	Instrument Ops	Cross-Link	Pre-Heating	Firing
Power Usage (W)	11	28	52	31	17
Duration (hr)	...	4	8	0.5	0.3

Solar panels consisting of 12 coplanar strings, each with 7 cells generating approximately 0.8 W per cell at the beginning of life (BOL), would generate 62.5 W at BOL and satisfy the power requirements. The strings would be attached to two gimbaled, deployable solar panels similar to the HaWK array used by the JPL mission MarCO. The sizing was based on the power modes, as well as a (conservative) assumption of an eclipse fraction of 40% throughout most modes, with 25% being assumed for data transmission (pointing towards Sun whenever possible). A worst case incident angle of 10° was also assumed.

Data transmission can be particularly power intensive, and the daughterships may undergo eclipses. A lithium-ion battery solution, consisting of eight batteries producing a total of 77 W hr would be sufficient for the assumed mission profile. A maximum of 60% depth of discharge was assumed in determining the number of batteries required.

7. Thermal Management

Primarily of concern in terms of thermal management would be the heat produced by the (X- or UHF-band) transmitter and ensuring that the temperature of both the propulsion unit and battery array would remain within operating limits. Given the volumetric constraints of a small spacecraft, primarily passive heat management would be employed, with radiators being placed on the external structure. Both the structure and secondary heatpipes would ensure the flow of energy to the radiators. Active heaters would be used for the battery array and propulsion system in order to maintain their temperatures within operating limits, but, in general, components would be placed in such a fashion that use of active thermal management units would be minimized. For instance, the battery array could be placed close to the transceiver, such that a portion of the heat generated by the transmitter could flow to the battery array over the structure.

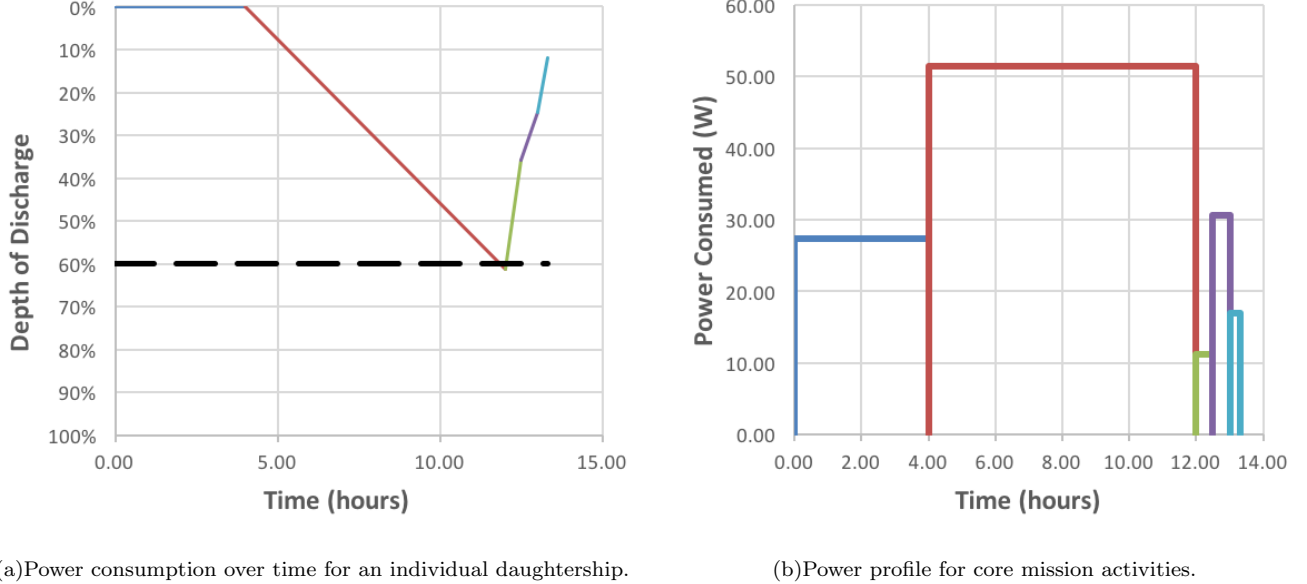


FIG. 19: Representative excerpts of the expected power profile and power consumption over time, including 30% contingency. The sole power negative mode (red) is related to cross-linking data.

8. Radiation and Shielding

For the proposed mission, the radiation requirements would be fairly modest, at least during nominal mission operations. Previous measurements have shown an average dose of 10 krad yr^{-1} to be expected in the selected orbit. Most currently available small spacecraft hardware is qualified to 50 krad, and most of the assumed RELIC electronics are capable of enduring a dose of up to 200 krad without additional shielding. For a mission duration of approximately 1 year, as well as the shielding provided by the structure, radiation is unlikely to be an issue. During transit to the final orbit, when the van Allen belts are traversed, additional shielding is provided by the transport craft, the deployment “pod,” and the undeployed solar panels.

B. Mothership Design

The mothership serves to accumulate the data streams from the individual daughterships and transmit them back to Earth. Primary drivers for the design of the mothership were the data storage and the communication subsystem. Our objective was to design a mothership as a small spacecraft with a mass of no more than 100 kg. Most of the subsystems have similar requirements as for the ones for the daughterships and would be similar. Key differences between the mothership and daughterships would be the telecommunications and data storage.

The telecommunications subsystem would have two components, one for receiving the data from the daughterships and one to transmit the collected data to the Earth. In order to receive the cross-links from the daughterships, the mothership would carry four receivers, each of which operates on a sub-band, allowing for simultaneous communication with daughterships. In order to communicate to Earth, the mothership would use a high-gain parabolic antenna operating in Ka band, allowing for data rates of up to 1.2 Gbps. Handling this volume of data may require upgrades to the current Deep Space Network (DSN) ground stations.

At least $32 \times 32 \text{ GB}$ of data storage are required to store all daughtership data (science data and housekeeping data). This volume exceeds available single chip configurations, but a RAID-0 array of FLASH NAND storage chips would be capable of handling this volume.

In order to reduce the amount of data downlinked to the ground, it would be attractive to do the interferometric correlation on the mothership. This solution requires very significant computing capabilities, which, in turn, require additional power. The most likely solution is a compromise when a very limited set of sources are correlated on the mothership, but the bulk of the data downlinked to Earth to be correlated on the ground by independent research groups using own CPU capabilities.

V. IMAGE RECONSTRUCTION

The act of combining the individual radio signals to form an image is an involved one for which there are several large dedicated software libraries such as AIPS and current industry standard, CASA [62]. However, for space based arrays, certain assumptions built into these libraries are broken. For instance, when generating Measurement Sets (MSs), CASA takes in initial positions for the array, but assumes that the only motions of the antennas are from the fixed rotation of the Earth. Normal ground based interferometers need to be aware of all the minute effects of Earth's orbit, from daily rotation to nutation and precession, in order to get the most exact separations between antennae (called baselines) for a given target in the sky. They use and update models of the separations to add the appropriate phase delays between signals so they can be added coherently and properly correlated. For an array that is in a dynamic orbit around the Earth or Moon, there is no existing software that can simulate its observations or process its data, so we filled the gap by precomputing the baselines in the correct frame and inserting them into the CASA MS file before the visibilities are computed with standard algorithms like CASA's `sm.predict()`. This also allows us to utilize the full range of CASA analysis functions, including CLEAN for forming an image from the simulated data.

Adding Baseline Tracking

For space based arrays, we are only concerned with the motion of the spacecraft in the orbit, which is fully captured by an orbit file in EME2000 coordinates. The simulated orbit determinations are made with GPS sidelobes and have an error associated with the recovered positions. These add phase noise to the visibilities, and corrupt the recovered image. This new noise source is included in our simulations. Given an RA and Declination of the source, we create a coordinate system $X'Y'Z'$, where Z' is pointing towards the source. RA and Dec are in the J2000 frame, which is identical to EME2000 for our purposes.

$$\begin{aligned} Z' &= (tx, ty, tz) \text{ where} \\ tx &= \cos(Dec) * \cos(RA) \\ ty &= \cos(Dec) * \sin(RA) \\ tz &= \sin(Dec) \end{aligned}$$

and RA and Dec are in radians.

X' is formed by taking $Z' \times Z$, which points parallel to lines of latitude and in the positive RA direction, and Y' completes the system, pointing parallel to lines of longitude and in the positive Dec direction.

The program parses the orbit file to get the 3 dimensional difference vectors of all the pairs of daughterships over a given period. It then projects these vector difference to the $X'Y'Z'$ frame. Dividing these projected differences by the user defined wavelength then gives the correct UVW coordinates for every baseline in the orbit for that particular source position. Our codes can also select multiple time windows from the orbit file to integrate over, providing maximum flexibility for operations scheduling testing. These coordinates are inserted into a CASA MS file after its creation, but before the radio visibilities are calculated.

Adding Noise

Most radio interferometry simulation software depends on the measurement equation, where Jones matrices are used to represent the measured voltage and sky brightness for a given baseline and model the noise effects happening to it with different operations on the matrix. Thermal noise is added directly to the brightness matrix, but for all other effects such as modeling the gain and phase errors the brightness matrix on the left and right are multiplied with the conjugate transposes of the transformation matrices. The resulting matrix is the voltage matrix which models what the actual measurements will be.

To calculate the root mean square, RMS, on the Gaussian thermal noise to add, one usually looks at the levels of different instrumental sources of noise [65]. But in this frequency range, the galactic noise is the major limiting factor. We used Cane's 1979 measurements in [9] to get the T_{sys} temperatures from the frequency dependent galactic noise, which is turned into noise RMS using the following formula:

$$\sigma = \frac{2k_B T_{sys}}{\eta_s A_{eff} \sqrt{N_a(N_a - 1) N_{pol} \tau \Delta\nu}}$$

Phase error will also be introduced in an orbiting array due to the uncertainty in the position of the daughterships, as well as differences in the clocks of the individual daughterships. The change in phase for a given positional error $d\tau$ is $2\pi\nu d\tau$.

From the full 3-D interferometry equation,

$$V_\nu(u, v, w) = \int \int I_\nu(l, m) e^{-2\pi i(ul+vm+wn)} dl dm.$$

The change in phase from a positional error $(du, dv, dw) = \frac{(dx, dy, dz)}{\lambda}$ and a clock error dt is

$$\begin{aligned} d\phi &= 2\pi\nu d\tau = 2\pi \frac{c}{\lambda} d\tau = 2\pi \left(du \cdot \ell + dv \cdot m + dw \sqrt{1 - \ell^2 - m^2} + dt \cdot \frac{c}{\lambda} \right) \\ \ell, m &\ll 1 \text{ for target images of less than a few degrees} \\ \implies \nu d\tau &\approx dw + dt \cdot \nu \\ \implies cd\tau &\approx dz + dt \cdot c, \text{ error in meters} \\ \implies d\tau &= \frac{dz}{c} + dt, \text{ error in seconds} \\ \implies d\phi &= 2\pi\nu d\tau = 2\pi\nu \left(\frac{dz}{c} + dt \right) = 2\pi \left(\frac{dz}{\lambda} + \nu dt \right) \end{aligned}$$

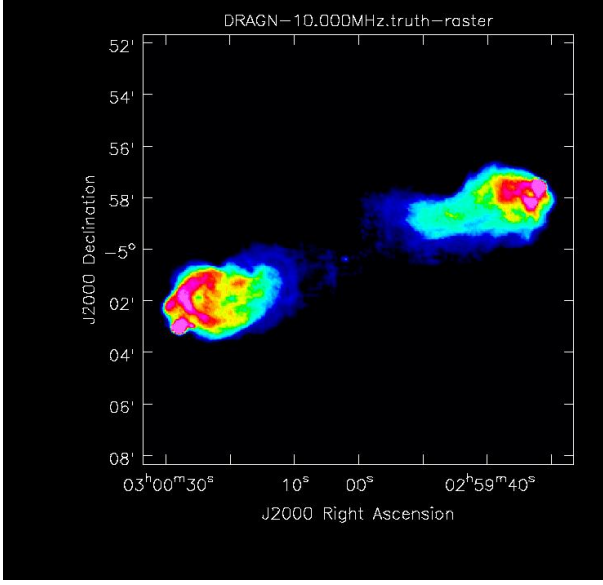
Given an RMS positional uncertainty of σ , assuming uncorrelated errors, we expect the uncertainty in the z direction of a single antenna to be $\sigma_z = \frac{\sigma}{\sqrt{3}}$. Then, since dz in question is for a baseline involving 2 antennas, we get dz by sampling a Gaussian distribution with $\sigma_z = \frac{\sigma\sqrt{2}}{\sqrt{3}}$. Then clock error dt is also sampled from a different Gaussian distribution with its own given RMS. With the given uncertainties, the software can then add the phase error by applying a rotation matrix to the complex gains, or, equivalently, to the final visibilities in the CASA MS file. The inversion of the visibilities to get the dirty image is then done with the usual 2D Inverse FFT, or can be treated with CASA's CLEAN function, which has many advanced features such as w-projection, which is useful for large images.

Imaging Performance

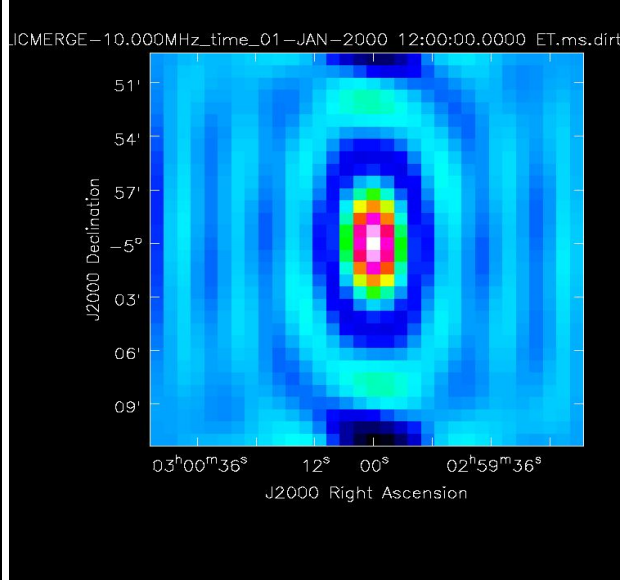
We were able to implement these features into an easily editable python code uploaded to <https://github.com/alexhege/SpaceCASA>. The following figures were created with this script to emulate the performance of the 32 element RELIC array. We tested an average DRAGN for the array, 100 arcsec wide, 100 Jy total brightness, and used a detailed picture of Cygnus A at 21 cm to provide realistic complexity to the truth image. We are integrating for 35 minutes, which is 2100 seconds, again a typical expectation. We assume a 5 nanosecond phase uncertainty per spacecraft, and galactic noise at 10 MHz. We are using CASA's CLEAN algorithm to create the image and have w-projection turned on. We have shrunk the baselines by a factor of 10, which gives us an image 10x larger than our prescribed 100 arcsec. This was done since CASA crashes if the baselines are too large. But the relative scales are the same, so it provides an accurate sense of RELIC's performance.

VI. DISCUSSION

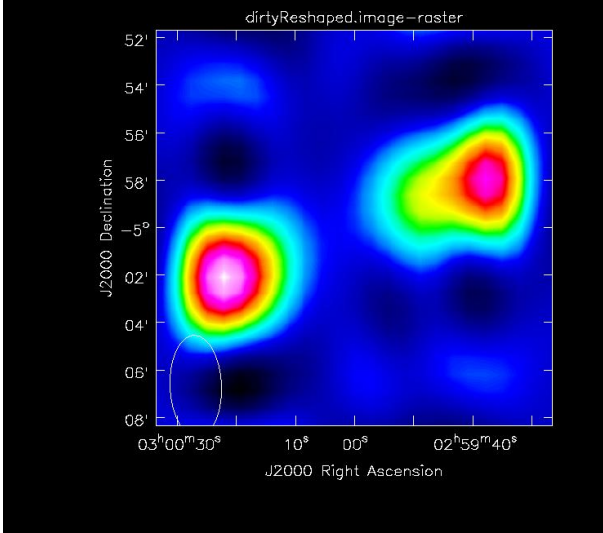
We described a proposed space-based decametric wavelength radio telescope aimed primarily for observation of radio galaxies. It leverages on existing small satellite technologies with the baseline mission consisting of one mothership and 32 daughterships with dual polarization antennas. Based on our analysis of the uv-plane coverage provided Section III B, the necessary integration times discussed at the beginning of Section II and the data downlink requirements discussed in Sections III D and III E, the proposed mission can fit under a standard two-year mission plan to fulfill the proposed scientific goals. The proposed space-based telescope being free from the influence of the Earth's ionosphere will become the key part of a multi-wavelength study of physical processes in the active galaxies and will become the primary tool for observing low-frequency phenomena from wide range of radio sources in the sky. The proposed mission is viable for implementation in the near term based missions manifested for launch in the next 5 years.



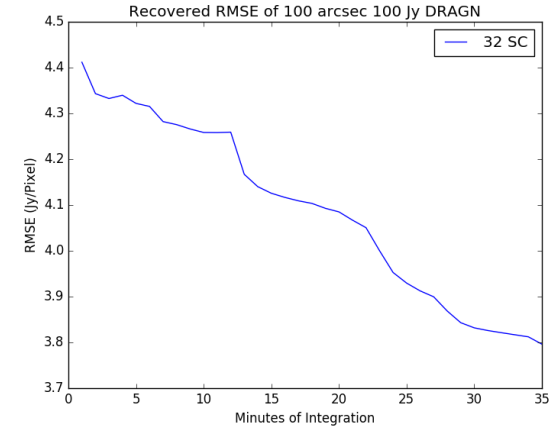
(a) Input image of realistic DRAGN, actually Cygnus A at 21 cm wavelength, scaled to 100 arcsec.



(b) Synthesized beam from point spread function after 35 minutes of integration



(c) Smoothed recovered image after 35 minutes of integration



(d) Root Mean Square Error between Truth and Recovered Image

FIG. 20: Images showing the CASA simulated performance of RELIC on a 100 arcsecond wide, 100 Jy total bright DRAGN. This was done with part of the orbit where the maximum baseline is 370 km, which corresponds to a resolution of roughly 15-20 arcsec.

Acknowledgments

We thank S. Murray and K. Weiler for their guidance and helpful comments at an early stage of this concept development as well as R. MacDowall for illuminating conversations. Some of the science motivation for the RELIC concept was articulated in “Small Satellites: A Revolution in Space Science” study co-led by Charles Norton, Sergio Pellegrino, and Michael Johnson at the W. M. Keck Institute for Space Studies. Part of this research was carried out at the Jet Propulsion Laboratory, California Institute of Technology, under a contract with the National Aeronautics

-
- [1] Jansky, K. G. 1935, *Proc. I. R. E.*, 23, 1158
 - [2] Ryle, M. & Vonberg, D. D. 1946, *Nature (London)*, 158, 339
 - [3] Pawsey, J. L., Payne-Scott, R., & McCready, L. L. 1946, *Nature (London)*, 157, 158
 - [4] McCready, L. L., Pawsey, J. L., & Payne-Scott, R. 1947, *Proc. Royal Soc. A*, 190, 357
 - [5] Ryle, M., Smith, F. G., & Elsemore, B. 1950, *MNRAS*, 110, 508
 - [6] Mills, B. Y. 1952, *Aust. J. Sci. Res.*, A5, 456
 - [7] Ryle, M. 1952, *Proc. Royal Soc. A*, 211, 351
 - [8] Reber, G., & Ellis, G. R. 1956, "Cosmic Radio-Frequency Radiation Near One Megacycle," *J. Geophys. Res.*, 61, 1
 - [9] Cane, H. V. 1979, "Spectra of the Non-Thermal Radio Radiation from the Galactic Polar Regions," *MNRAS*, 189, 465
 - [10] Ellis, G. R. A., & Mendillo, M. 1987, "A 1.6 MHz survey of the galactic background radio emission," *Aust. J. Phys.*, 40, 705
 - [11] Salas, P., Oonk, J. B. R., van Weeren, R. J., Salgado, F., Morabito, L. K., Toribio, M. C., Emig, K., Rottgering, H. J. A., & Tielens, A. G. G. M. 2017, *MNRAS*, in press
 - [12] *Handbook Radio Astronomy*, Second Edition, International Telecommunications Union, Geneva, 2004.
 - [13] Bougeret, J.-L., Kaiser, M. L., Kellogg, P. J., et al. 1995, "Waves: The Radio and Plasma Wave Investigation on the Wind Spacecraft," *Space Sci. Rev.*, 71, 231; doi: 10.1007/BF00751331
 - [14] Gurnett, D. A., Kurth, W. S., Kirchner, D. L., et al. 2004, "The Cassini Radio and Plasma Wave Investigation," *Space Sci. Rev.*, 114, 395; doi: 10.1007/s11214-004-1434-0
 - [15] Bougeret, J. L., Goetz, K., Kaiser, M. L., et al. 2008, "S/WAVES: The Radio and Plasma Wave Investigation on the STEREO Mission," *Space Sci. Rev.*, 136, 487; doi: 10.1007/s11214-007-9298-8
 - [16] Kurth, W. S., Kirchner, D. L., Hospodarsky, G. B., et al. 2012, "The Juno Waves investigation," *European Planetary Science Congress 2012*, id. EPSC2012-281; <http://meetings.copernicus.org/epsc2012>
 - [17] Alexander, J. K., Brown, L. W., Clark, T. A., Stone, R. G., & Weber, R. R. 1969, "The Spectrum of the Cosmic Radio Background Between 0.4 and 6.5 MHz," *ApJ*, 157, L163
 - [18] Alexander, J. K., Kaiser, M. L., Novaco, J. C., Grena, F. R., & Weber, R. R. 1975, "Scientific instrumentation of the Radio-Astronomy-Explorer-2 satellite," *A&A*, 40, 365
 - [19] Swarup, G. 1990, "Giant metrewave radio telescope (GMRT) - Scientific objectives and design aspects," *Indian J. Radio Space*, 19, 493
 - [20] Ananthakrishnan, S. 1995, "The Giant Meterwave Radio Telescope / GMRT," *J. Astrophys. Astron.*, 16, 427
 - [21] Kassim, N. E., Lazio, T. J. W., Erickson, W. C., Perley, R. A., Cotton, W. D., Greisen, E. W., Cohen, A. S., Hicks, B., Schmitt, H. R., & Katz, D. 2007, "The 74 MHz System on the Very Large Array," *ApJS*, 172, 686
 - [22] Braude, S. Ia., Megn, A. V., Riabov, B. P., Sharykin, N. K., & Zhuk, I. N. 1978, "Decametric survey of discrete sources in the Northern sky. I - The UTR-2 radio telescope: Experimental techniques and data processing," *Ap&SS*, 54, 3
 - [23] van Haarlem, M. P., et al. 2013, "LOFAR: The LOw-Frequency ARray," *A&A*, 556, A2
 - [24] Ellingson, S. W., Taylor, G. B., Craig, J., et al. 2013, "The LWA1 Radio Telescope," *IEEE Trans. Ant. Prop.*, 61, 2540; doi: 10.1109/TAP.2013.2242826
 - [25] Taylor, G. B., Ellingson, S. W., Kassim, N. E., et al. 2012, "First Light for the First Station of the Long Wavelength Array," *J. Astron. Instrum.*, 1, 1250004; doi: 10.1142/S2251171712500043
 - [26] Tingay, S. J., et al. 2013, "The Murchison Widefield Array: The Square Kilometre Array Precursor at Low Radio Frequencies," *Publ. Astron. Soc. A.*, 30, 7
 - [27] French, F. W., Huguenin, G. R., & Rodman, A. K. 1967, "A synthetic aperture approach to space-based radio telescopes," *J. Spacecraft Rockets*, 4, 1649
 - [28] Weiler, K. W., Johnston, K. J., Simon, R. S., Dennison, B. K., Erickson, W. C., Kaiser, M. L., Cane, H. V., & Desch, M. D. 1988, *A&A*, 195, 372
 - [29] Basart, J. P., Burns, J. O., Dennison, B. K., Weiler, K. W., Kassim, N. E., Castillo, S. P., & McCune, B. M. 1997a, "Directions for space-based low frequency radio astronomy. 1. System considerations," *Radio Sci.*, 32, 251
 - [30] Basart, J. P., Burns, J. O., Dennison, B. K., Weiler, K. W., Kassim, N. E., Castillo, S. P., & McCune, B. M. 1997b, "Directions for Space-Based Low-Frequency Radio Astronomy 2. Telescopes," *Radio Sci.*, 32, 265
 - [31] Oberoi, D., & Pinçon, J.-L. 2005, *Radio Sci.*, 40, 4004
 - [32] Jones, D. L., et al. 2000, "The ALFA Medium Explorer Mission," *Adv. Space Res.*, 26, 743
 - [33] Banazadeh, P., Lazio, J., Jones, D., Scharf, D. P., Fowler, W., & Aladangady, C. 2013, "Feasibility analysis of XSOLANTRA: A mission concept to detect exoplanets with an array of CubeSats," in *Proc. 2013 IEEE Aerospace Conf.*; doi: 10.1109/AERO.2013.6496864
 - [34] R. T. Rajan, S. Engelen, M. Bentum and C. Verhoeven, 2011, "Orbiting Low Frequency Array for radio astronomy," in *Proc. 2011 Aerospace Conference*, 1-11, doi=10.1109/AERO.2011.5747222
doi: 10.1109/AERO.2016.7500678
 - [35] A. J. Boonstra et al, "Discovering the sky at the Longest Wavelengths (DSL)," in *Proc. 2016 IEEE Aerospace Conference, Big Sky, MT*, 2016, pp. 1-20.

- [36] B. Cecconi et al., "NOIRE Study Report: Towards a Low Frequency Radio Interferometer in Space," In Proc. 2018 IEEE Aerospace Conference, arXiv:1710.10245
- [37] Baumbach, M. M., Gurnett, D. A., Calvert, W., & Shawhan, S. D. 1986, "Satellite interferometric measurements of auroral kilometric radiation," *Geophys. Res. Lett.*, **13**, 1105
- [38] Mutel, R., Gurnett, D. A., & Christopher, I. 2004, "Spatial and Temporal Properties of AKR Burst Emission Derived From Cluster WBD VLBI Studies," *Annales Geophys.*, **22**, 2625
- [39] Norton, C. D., Pellegrino, S., Johnson, M., et al. 2014, "Small Satellites: A Revolution in Space Science," W. M. Keck Institute for Space Studies; <http://kiss.caltech.edu/study/smallsat/KISS-SmallSat-FinalReport.pdf>
- [40] Kassim, N. E., & Weiler, K. W. 1990, *Low frequency astrophysics from space*, Lecture Notes in Physics, Vol. 362 (Springer-Verlag: Berlin)
- [41] Stone, R. G., Weiler, K. W., Goldstein, M. L., & Bougeret, J.-L. 1998, *Radio Astronomy at Long Wavelengths*, Geophysical Monograph Series, Vol. 119 (American Geophysical Union: Washington, DC) ISSN 0065-8448
- [42] Harris, D. E. 2005, "From Clark Lake to Chandra: Closing in on the Low End of the Relativistic Electron Spectra in Extragalactic Sources," in *From Clark Lake to the Long Wavelength Array: Bill Erickson's Radio Science*, Astron. Soc. Pacific Conference Series, Vol. 345, eds. N. Kassim, M. Perez, M. Junor, & P. Henning (Astron. Soc. Pacific: San Francisco) p. 254
- [43] Ineson, J., Croston, J. H., Hardcastle, M. J., & Mingo, B. 2017, "A representative survey of the dynamics and energetics of FR II radio galaxies," *MNRAS*, in press
- [44] R. Laing, J. Riley and M. Longair, *Bright radio sources at 178 MHz: Flux densities, optical identifications and the cosmological evolution of powerful radio galaxies*, *Mon. Not. R. astr. Soc.*, **204**, 151-187 (1983).
- [45] J. P. McKean et al., *LOFAR imaging of Cygnus A ? direct detection of a turnover in the hotspot radio spectra*, *Mon. Not. R. astr. Soc.*, **463**, 3, 3143?3150 (2016).
- [46] M. Klein Wolt et al., *Radio astronomy with the European Lunar Lander: Opening up the last unexplored frequency regime*, *Planetary and Space Science*, **74**, 1, 167-178 (2012).
- [47] L. Chen et al., *Antenna design and implementation for the future space Ultra-Long wavelength radio telescope*, submitted to Experimental Astronomy, arXiv:1802.07640
- [48] J.M. Cordes, *Low frequency interstellar scattering and pulsar observations*, in *Low frequency astrophysics from space; Proceedings of an International Workshop*, Crystal City, VA, Jan. 8, 9, 1990 (A91-57026 24-89). Berlin and New York, Springer-Verlag, 165-174 (1990).
- [49] S.Ya. Braude et al, *Decametric survey of discrete sources in the northern sky*, *Astrophys and Sp. Sci.*, **280** 3, 235–300 (2002).
- [50] S. Chien, G. Rabideau, R. Knight, R. Sherwood, B. Engelhardt, D. Mutz, T. Estlin, B. Smith, F. Fisher, T. Barrett, G. Stebbins, Aspen?automated planning and scheduling for space mission operations. InSpace Ops 2000 June, Toulouse, France, AIAA.
- [51] S.A. Chien, R. Knight, A. Stechert, R. Sherwood, G. Rabideau, "Using Iterative Repair to Improve the Responsiveness of Planning and Scheduling," In *Artificial Intelligence Planning Systems*, 2000 Apr (pp. 300-307), AAAI Press.
- [52] C.H. Acton, "Ancillary Data Services of NASA's Navigation and Ancillary Information Facility," *Planetary and Space Science*, Vol. 44, No. 1, pp. 65-70, 1996.
- [53] Mills, B. Y. 1953, "The Radio Brightness Distributions over Four Discrete Sources of Cosmic Noise," *Aust. J. Phys.*, **6**, 452
- [54] Blythe, J. H. 1957, "A new type of pencil beam aerial for radio astronomy," *MNRAS*, **117**, 644
- [55] Ryle, M., & Hewish, A. 1960, "The synthesis of large radio telescopes," *MNRAS*, **120**, 220
- [56] Bell, D., Satorius, E., Kuperman, I., & Koenig, J. 2014, "Multiuser Receiver Architectures for Space Modems," *The Interplanetary Network Progress Report*, vol. 42-198 (Jet Propulsion Laboratory, California Institute of Technology: Pasadena, CA) p. 1-13
- [57] B. Porat, *A Course in Digital Signal Processing*, John Wiley and Sons, New York, 1997.
- [58] *Pseudo-Noise and Regenerative Ranging*, Deep Space Network No. 810-005 214, Rev A, October 28, 2015
- [59] J. Berner, S. Bryant, P. Kinman, *Range Measurement as Practiced in the Deep Space Network*, Proceedings of the IEEE, Vol. 95, No. 11, November 2007.
- [60] K. Andrews J. Hamkins, S. Shambayati, V. Vilnrotter, *Telemetry-Based Ranging*, Proceedings of the 2010 IEEE Aerospace Conference, Big Sky, MT, March 2010.
- [61] Thompson, A. R., Moran, J. M., & Swenson, G. W. 2007, *Interferometry and Synthesis in Radio Astronomy*, (Wiley: New York)
- [62] McMullin, J. P., Waters, B., Schiebel, D., Young, W., and Golap, K. 2007, *Astronomical Data Analysis Software and Systems XVI (ASP Conf. Ser. 376)*, ed. R. A. Shaw, F. Hill, D. J. Bell (San Francisco, CA: ASP), 127
- [63] Kocz, J., Greenhill, L. J., Bardsell, B. R., Price, D., Bernardi, G., Bourke, S., Clark, M. A., Craig, J., Dexter, M., Dowell, J., Eftekhari, T., Ellingson, S., Hallinan, G., Hartman, J., Jameson, A., MacMahon, D., Taylor, G., Schinzel, F., & Werthimer, D. 2015, "Digital Signal Processing Using Stream High Performance Computing: A 512-Input Broadband Correlator for Radio Astronomy," *J. Astron. Instrumentation*, **4**, 1550003; doi: 10.1142/S2251171715500038
- [64] I. Marti-Vidal, *Aperture Synthesis Simulator for Radio Astronomy*, <https://launchpad.net/apsynsim>
- [65] S. Ellingson, *Sensitivity of Antenna Arrays for Long-Wavelength Radio Astronomy*, IEEE Transactions on Antennas and Propagation (2010).
- [66] Zurbuchen, T. H., Bhavya Lal, B., et al. 2016, *Achieving Science with CubeSats: Thinking Inside the Box* (National Academies Press: Washington, DC) ISBN: 978-0-309-44263-3

- [67] N.Meyer-Vernet and C.Perche *Tool Kit for Antennae and Thermal Noise Near the Plasma Frequency*, Journal of Geophysical Research, 94, 2405 ? 2415, (1989).
- [68] A.Zaslavsky et al., *On the antenna calibration of space radio instruments using the galactic background: General formulas and application to STEREO/WAVES*, Radio Science, 46, RS2008 (2011).
- [69] James, H. G., King, E.P., White, A., Hum, R. H., Lunscher, W. H. H. L., Siefring, C. L., *The e-POP Radio Receiver Instrument on CASSIOPE*, Space Sci Rev, 189, 79-105 (2015).

Appendix A: RELIC HF Antenna and Front-End Design

While the detailed description of the science data acquisition hardware is beyond the scope of this paper, it is nonetheless an integral part of the mission concept description and it is also responsible for generating the raw science data that are then transmitted by the daughter ships (which is much of the focus of this paper). Accordingly, we present here a brief description of how the science data acquisition hardware for RELIC might look.

1. Objectives

The objective of this is to characterize the antenna length and front-end impedance parameters that provide a background-noise-limited system for the RELIC antenna. The RELIC signals will be wide-band measurements across the 0.1-30 MHz band. The overall desired performance is 1) that the antenna noise be greater than the amplifier noise, 2) stable gain in each sub-band, 3) smooth gain and phase variations across the band, 4) reducing too much variation of gain across the band so that dynamic range is not an issue. The scope of this document is to identify a solution for a high-impedance input design that primarily aims to meet point 1 but with points 2-4 in mind.

2. Assumptions

a. Antenna Model

The band of interest for RELIC extends from 0.1 – 30 MHz. Below 1 MHz, the galactic noise is low but “shot noise” due to the plasma environment is dominant. The antenna models used for the initial assessment are 6-meter and 5-meter full length dipoles made of 0.6 cm ($\sim 0.25''$) diameter copper. The antennas are modeled using NEC2. The directivity, impedance (real and imaginary) along with the phase and group delay are shown in Figure 21.

b. Background Noise

The galactic noise is modeled according to the parametrization described in [9]. A plot of the average galactic noise temperature is shown in Figure 22

The noise-voltage-squared spectrum at the antenna terminals due to galactic noise is given by $V_{A,gal}^2 = 4k_B T_{gal} R_{ant}$, where k_B is Boltzmann’s constant and R_{ant} is the real part of the antenna impedance. In addition to galactic noise, there is a “shot noise” contribution due to electrons in the plasma colliding with the antenna and inducing currents [67]. The noise-voltage-squared contribution as parameterized by [68] is given by:

$$V_{A,QTN}^2 = 5 \times 10^{-5} \frac{V^2}{Hz} \times \left(\frac{n_e}{cm^{-3}} \right) \times \left(\frac{T_e}{K} \right) \times \left(\frac{f}{Hz} \right)^3 \times \left(\frac{L/2}{m} \right)^{-1}, \quad (A1)$$

where n_e is the plasma frequency in electrons per cm^3 , T_e is the electron plasma temperature in Kelvin, f is the frequency in Hz, and L is the full dipole length in meters. We assume $n_e = 5 cm^{-3}$ and $T_e = 10^5$ Kelvin. The background noise-voltage-squared contributions are shown for a modeled 6-meter (full length) and a 5-meter dipole made of 0.6 cm diameter copper rod in Figure 23.

3. Analysis

The goal is to estimate the sources of noise at the first amplifier in the signal chain to ensure the noise is dominated by external backgrounds rather than by the amplifier itself. The external noise sources producing voltages at the antenna terminals will produce a voltage at the load according to

$$V_L = \frac{Z_L}{Z_A + Z_L} V_A, \quad (A2)$$

where Z_L is the complex impedance of the load and Z_A is the antenna impedance. The noise due to the amplifier, at the load is given by $V_{L,amp}^2 = k_B T_{amp} R_{amp}$. We consider an operation amplifier (OpAmp) approach for producing a high-input impedance to the amplifier as seen from the terminals of the antenna.

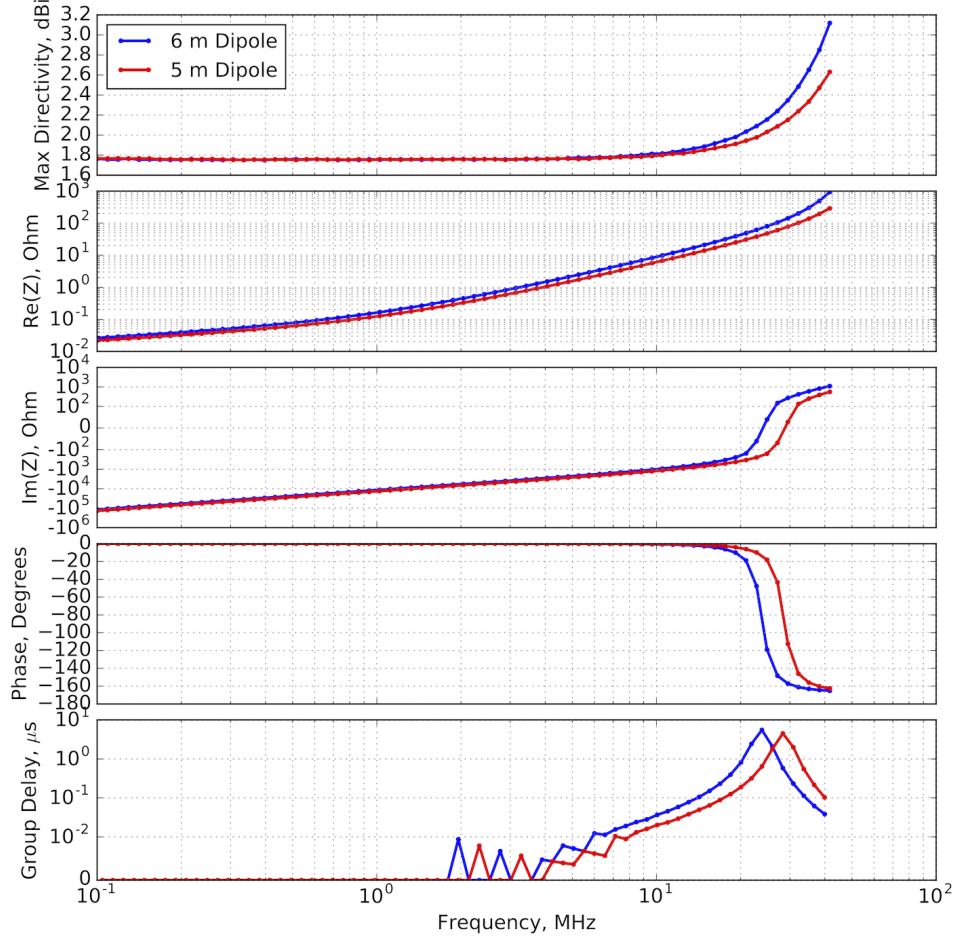


FIG. 21: NEC2 models of a 6-meter and 5-meter full-length dipole. The model assumes the antenna is made of copper rod with 0.6 cm diameter floating in free space.

OpAmps can be designed to have a high input impedance but modeling their noise is somewhat more involved. A modeling effort using an OpAmp was done for JPL's Universal Space Transponder (UST) Jovian burst science application development. Figure 24 is an OPA656-based design by Robert Dengler for the Universal Space Transponder (UST) using 12.7 k Ω input impedance (set by R8 in Figure 24).

For this application, we considered the OPA656 from Texas Instruments. The choice is driven by the noise characteristics $V_n = 7\text{nV}/\sqrt{\text{Hz}}$, $I_n = 1.3\text{fA}/\sqrt{\text{Hz}}$. The low current noise is particularly important for these high impedance applications. It is worth mentioning the e-POP radio receiver instrument on CASSIOPE also used OPA656 for its receiver with a 100M Ω input impedance [69].

Based on the Analog Devices Tutorial MT-049, adapted to the notation on our circuit diagram, the noise model is calculated according to:

$$V_{L,amp}^2 = V_n^2 + I_n^2 Z_+^2 + I_n^2 \left(\frac{R_3 R_4}{R_3 + R_4} \right) + 4kT_0 \left(R_e(Z_+) + R_3 \left(\frac{R_4}{R_3 + R_4} \right)^2 + R_4 \left(\frac{R_3}{R_3 + R_4} \right)^2 \right), \quad (\text{A3})$$

where Z_+ is the lump impedance seen from the terminal labeled “+”, including the antenna impedance and T_0 is the physical temperature of the resistors, taken to be room temperature $T_0 = 290$ Kelvin. The last term in curly brackets is the Johnson noise of the system. The different noise terms, assuming $R_8 = 12.8, 50$ and $100\text{k}\Omega$, are shown below. The different noise contribution, for a 5-meter antenna, are shown in Figure 25. In all cases V_n is, by far, the dominant source of noise.

Simulations were run to obtain the impedance as a function of frequency for 12.8 k Ω , 50 k Ω , and 100 k Ω , simply

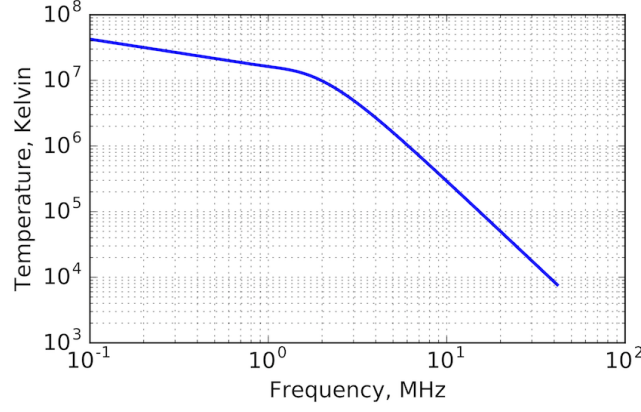


FIG. 22: The galactic noise temperature from the parameterization in [9].

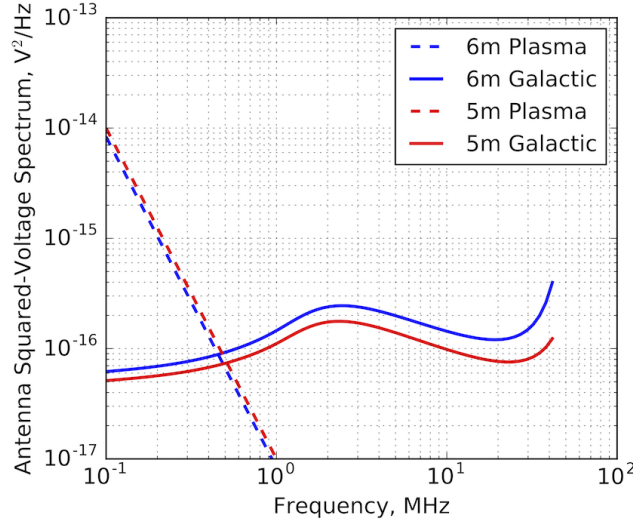


FIG. 23: The noise-squared voltage at the antenna terminals for the plasma shot noise contribution and the galactic noise. The noise is modeled for a 6 m and 5m full-length dipole.

by changing R8 in the design. The impedance of the amplifier as seen by the terminals of the antenna, is shown in Figure 26.

This OpAmp design has an impedance that is high at low frequencies and lower at high frequencies, which is the general desired direction for keeping the antenna noise above the amplifier noise across the band. The voltage at the load is given by:

$$\langle v_L^2 \rangle = \langle v_A^2 \rangle \frac{|Z_L|^2}{|Z_L + Z_A|^2}, \quad (\text{A4})$$

where Z_L is the impedance shown in Figure 26. The results for the antenna noise compared to the amplifier noise for the impedances considered here are shown in Figure 27.

The results of the OpAmp approach indicate that the OpAmp has a higher antenna to amplifier noise ratio. The reason points to the impedance vs frequency of the OpAmp, which has a profile with high impedance at low frequencies and low impedance at higher frequencies. This is the general behavior needed for the antenna noise to dominate across the band. We also note that using an OPA656 impedance with R8 resistor value $> 50 \text{ k}\Omega$ meets the desired design objectives laid out in the introduction. The antenna noise is above the amplifier noise with smooth behavior across the band that is not highly variable. The expected noise levels below 1 MHz can be as > 10 times higher than parts of the band above 1 MHz. However, frequencies below 1 MHz account for $< 10\%$ of the full band.

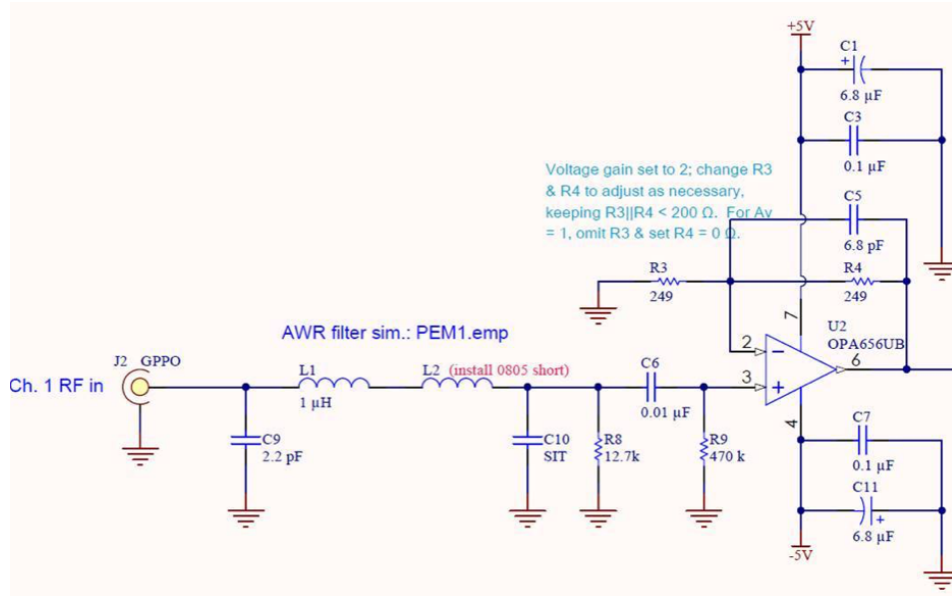


FIG. 24: Operational Amplifier front end design by Bob Dengler for the Universal Space Transponder.

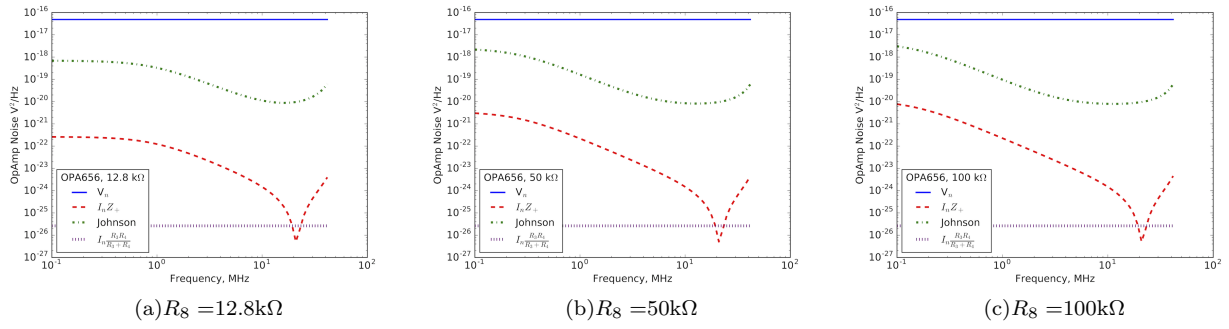


FIG. 25: The operational amplifier noise assuming different input impedance values. The noise is dominated by the voltage term regardless of the impedance used in the range considered. These simulations are for the 5-meter antenna only.

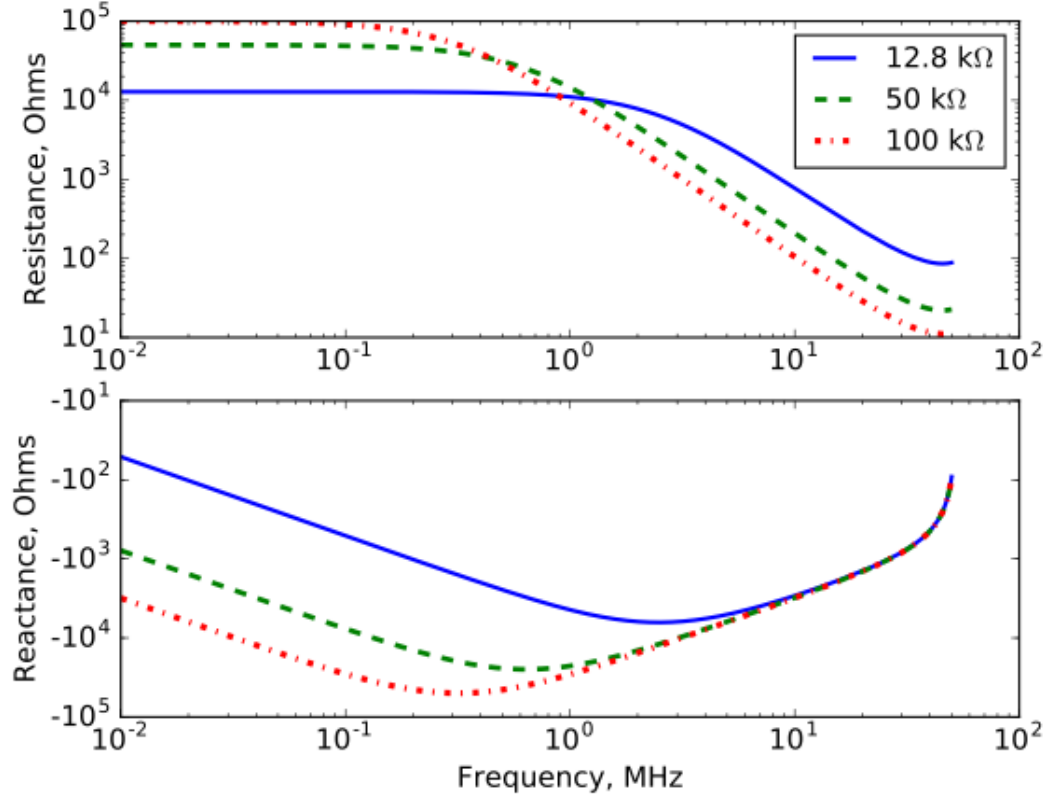


FIG. 26: Simulations of the impedance seen by the antenna terminals looking into the front-end design in Figure 24 for R_8 equal to 12.8, 50, and 100 k Ω .

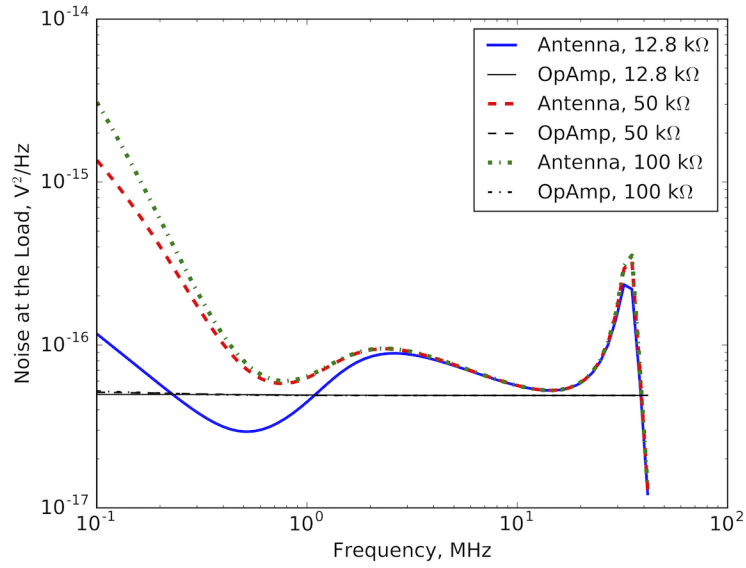


FIG. 27: Results for the noise due to the antenna and the amplifier noise for the front-end design in Figure 24 assuming values of R_8 equal to 12.8, 50, 100 k Ω .